Chem Soc Rev

Raman and Infra-Red Microspectroscopy: Towards Quantitative Evaluation for Clinical Research by Ratiometric Analysis

Journal:	*Chemical Society Reviews*
Manuscript ID	CS-REV-07-2015-000540.R1
Article Type:	Review Article
Date Submitted by the Author:	22-Sep-2015
Complete List of Authors:	Kumar, Srividya; Indian Institute of Science, Inorganic and Physical Chemistry Verma, Taru; Indian Institute of Science, Bioengineering Mukherjee, Ria; Indian Institute of Science, Inorganic and Physical Chemistry Ariese, Freek; Indian Institute of Science, Inorganic and Physical Chemistry; Vrije Universiteit, Laserlab Somasundaram, Kumaravel; Indian Institute of Science, Microbiology and Cell biology; Umapathy, Siva; Indian Institute of Science, Inorganic and Physical Chemistry; Indian Institute of Science, Instrumentation and Applied Physics

Raman and Infra-Red Microspectroscopy: Towards Quantitative Evaluation for Clinical Research by Ratiometric Analysis

Srividya Kumar[1], Taru Verma[4], Ria Mukherjee[1], Freek Ariese[1, 5], Kumaravel Somasundaram[3] and Siva Umapathy[1, 2,*]

[1]*Department of Inorganic and Physical Chemistry, Indian Institute of Science, Bengaluru 560 012, India*
[2]*Department of Instrumentation and Applied Physics, Indian Institute of Science, Bengaluru 560 012, India*
[3]*Department of Microbiology and Cell Biology, Indian Institute of Science, Bangalore 560 012, India*
[4]*Centre for Biosystem Science and Engineering, Indian Institute of Science, Bangalore-560012, India*
[5]*On leave from LaserLaB, Faculty of Sciences, VU University Amsterdam, 1081 HV Amsterdam, The Netherlands*
**For correspondence. (e-mail: umapathy@ipc.iisc.ernet.in)*

ABSTRACT

Biomolecular structure elucidation is one of the major techniques for studying the basic processes of life. These processes get modulated, hindered or altered due to various causes like diseases, which is why biomolecular analysis and imaging can play an important role in diagnosis, treatment prognosis and monitoring. Vibrational spectroscopy (IR and Raman), which is a molecular bond specific technique, can assist the researcher in chemical structural interpretation. Based on the combination with microscopy, vibrational microspectroscopy is currently emerging as an important tool for biomedical research, with a spatial resolution at the cellular and sub-cellular level. These techniques offer various advantages, enabling label-free, biomolecular fingerprinting in the native state. However, the complexity involved in deciphering the required information from a spectrum hampered their entry into the clinic. Today with the advent of automated algorithms, vibrational microspectroscopy excels in the field of spectropathology. However, researchers should be aware of how quantification based on absolute band intensities may be affected by instrumental parameters, sample thickness, water content, substrate background and other possible artefacts. In this review these practical issues and their effects on the quantification of biomolecules will be discussed in detail. In many cases ratiometric analysis can help to circumvent these problems and enable the quantitative study of biological samples, including ratiometric imaging in 1D, 2D and 3D. We provide an extensive overview from the recent scientific literature on IR and Raman band ratios used for studying biological systems and for disease diagnosis and treatment prognosis.

INTRODUCTION

Towards the end of the 20th century vibrational spectroscopy (based on Infra-Red absorption or Raman scattering), originally a physical chemistry technique for deducing the structure of molecules, has become a powerful tool in biomedical research. The foremost benefit provided by vibrational spectroscopy is that it can fingerprint the complete bio-molecular composition of a system in its native state without the need for labelling, extraction or purification[1, 2]. With the aid of optical microscopy, vibrational spectroscopy has moved into the field of chemical imaging. In a clinical setting, Infra-Red (IR) or Raman chemical images along with hyper-cluster analysis are becoming equivalent to the interpretation of microscopy images by pathologists. This may lead to a higher level of automation in diagnosis, thereby reducing human error and operator-dependent discrepancies. The strength of vibrational microspectroscopy in the biomedical field is based on the fact that morphological and functional changes resulting from any abnormality or ailment are always accompanied by biochemical changes. These changes occur along with or ahead of morphological changes. Thus, vibrational spectroscopy holds potential to fulfil a clinician's dream of "Early Diagnosis" for many ailments.

Vibrational micro-spectroscopy requires a spectrometer combined with an optical microscope[1, 2]. The former is used to disperse the light into its frequency components and the latter is used to spatially resolve biological entities. A microscope is not required for pure samples or homogeneous mixtures, where the spatial resolution has no relevance. Nevertheless, for Raman spectroscopy a microscope is often preferred to improve the light collection efficiency. Both IR and Raman spectra originate from bond vibrations of molecules, thereby making them specific to the biochemical composition. Detailed accounts on the principles, instrumentation, pre-processing methods and data analysis for Raman and Infra-red spectroscopy are given elsewhere[3-10]. A complete collection of band assignments for IR and Raman spectroscopy of biological systems was compiled by Movasaghi and co-workers[7, 8]. Byrne *et al.* described the challenges that vibrational spectroscopists need to face when moving from the research bench to the clinic to set up a "Division of Spectropathology"[9]. Gautam and co-workers[2] have reviewed the recent developments in instrumentation and data analysis procedures for Raman and IR imaging. Oladepo *et al.* have demonstrated a way to study the protein folding problem with the help of UV Resonance Raman Spectroscopy[11]. Various Surface Enhanced Raman Spectroscopy (SERS)

methodologies for the identification of bacteria, as well as other Raman techniques for clinical applications have been demonstrated by Popp and co-workers[5, 12]. Lyng *et al*. have described the application of Raman and IR microspectroscopy for screening of cancer, especially for oral and cervical cancer[13]. Lin and co-workers have given an account of diagnostic methods for a wide range of diseases, based on analysing tissues with Raman and IR microspectroscopy[14]. Shaw and Mantsch[15] described clinical diagnostic methods involving body fluid analysis with the help of IR spectroscopy.

The advent of user friendly algorithms has enabled the handling of large datasets produced during vibrational spectroscopy and imaging. Although multivariate analysis helps in classification and clustering of data, deducing a biochemically meaningful quantitative parameter from these models is not straightforward. Current clinical methodologies for body fluid profiling rely on quantitative parameters with set thresholds to distinguish between normal and abnormal conditions[16]. Hyper-cluster analysis of image data from biopsy sections is becoming equivalent to pathological assessments[17-19], whereas univariate analysis on a spectrum paves the way towards quantification. The term “univariate” refers to a single variable. For instance, investigating peak shifts, peak heights or peak shapes are methodologies for univariate spectroscopic analysis. Each entity provides insight into the structure of molecules under examination. For example, peak shifts identify the effect of isotope substitution, peak heights i.e. intensity changes can be directly correlated to the amount of target compound within the focal volume and peak shapes help to elucidate the hydrogen bonding nature of the system[20]. Peak shifts and peak shapes can help spectroscopists to better interpret results, but deriving a quantitative parameter would be complex. In contrast, intensities can be a parameter for quantification. The major drawback is that the intensity can be modulated not only by a change in the concentration but also due to various experimental factors like instrument fluctuations or slow drift, baseline modulations etc. These aspects will be discussed in more detail below. Figure 1 depicts the steps involved in spectral analysis. The choice between univariate and multivariate analysis depends on the objective of the study. It is advisable to perform univariate analysis when quantification of biomolecules is preferred. For instance, a ratio of the wavenumbers 1445 cm^{-1} (CH_2 bending) and 1655 cm^{-1}(Amide I) in Raman spectroscopy has been employed in cancer detection[21]. This ratio corresponds with the lipid to protein ratio. Multivariate analysis is more suited for studies or applications that require classification. For example, grading of cancer using biopsy sections where the pseudo coloured spectral maps are equivalent to staining

methodologies[22]. Furthermore, when the differences between groups are not obvious, multivariate analysis can aid in highlighting the subtle biochemical differences between them[23-25].

One of the easier ways to circumvent the problems associated with intensity measurements is to divide the value by a similar parameter that experiences identical fluctuations. As a result the artefacts get cancelled out, thus revealing the true biochemical changes. This process of dividing an intensity value of a peak with another in the same spectrum is called ratioing. Not only the intensity (peak height), but also the area under the peak or region can be analysed by ratioing. These ratio values help in the relative quantification of the different biomolecules, for example, the protein/lipid ratio which can act as a marker for the differentiation of cells in various growth phases as stated by Mourant *et al.*[26], or to monitor sepsis infection in mice using FTIR spectroscopy as reported by Gautam *et al*[27]. Such ratios can not only help in relative quantification but can also provide insight into the conformational changes occurring in biomolecules. For instance, in Raman spectra of proteins the ratio of the 1667 cm^{-1} band which corresponds to β-sheets or random coils and the 1656 cm^{-1} band which corresponds to α-helix, provides insight into protein folding or denaturation processes[6]. The value obtained by ratioing with well-defined thresholds also has the prospect of becoming a quantitative parameter for medical diagnosis. Here, the advantages, methodologies and effects of ratioing will be explained in detail with examples from our laboratory. To the best of our knowledge, this review is the first of its kind to specifically discuss the various approaches of ratiometric analysis. We also compiled a detailed library of ratios reported in the literature for both IR and Raman spectroscopic analyses in biomedical research.

MATERIALS AND METHODS

The spectra that we will use to illustrate the various ratiometric approaches were obtained in our laboratory. Raman experiments were performed using a Renishaw InVia Raman upright microscope (Renishaw Inc., U.K) and Raman grade CaF_2 windows (Crystan Optics, U.K). IR experiments were performed using a Varian UMA 600 Microscope (Agilent Technologies, U.S.A) and Kevley Low e slides (Varian Inc., MA). Raman spectral pre-processing and image analysis was performed using WiRE 4.1 (Renishaw Inc., U.K) and Origin 8.5 (Origin Labs, U.S.A). All graphs were created using GraphPad Prism 5(GraphPad Software Inc., U.S.A). IR images were analysed using Cytospec 1.3. The pre-processing applied for each

illustration is mentioned in their respective figure legends. The assignments for the peaks used for analysis in the illustrations are also indicated in the figure legends. The peak ratios were selected for demonstration purposes only.

RATIOMETRIC ANALYSIS

For a reliable quantitative analysis and to appreciate the usefulness of ratiometric analysis, it is of crucial importance to understand the experimental factors that may influence spectroscopic peak intensities. Various factors are discussed in detail in the sections below.

(A) Instrumental variability:

Several instrumental fluctuations can arise in a spectrometer that can result in erroneous data being generated. These fluctuations can come from source variations like ageing, improper functioning/alignment or incorrect focusing. In addition, the response function of the spectrometer and detector sensitivity varies for different wavelengths as well as for different optical elements or different instruments. In Raman, the fundamental intensity depends on the frequency of excitation and that of the particular vibration. Wavenumber calibration is a prerequisite before the start of any experiment. A detailed description of these aspects for Raman spectroscopy can be found in McCreery's book[28]. Similarly, Griffiths and Haseth have extensively described FTIR instrumentation, calibrations *etc* in their book[29]. Figure 2 illustrates how instrumental parameters such as laser power or alignment can affect the absolute intensities of a Raman spectrum but not the ratio of the concerned peaks. Raman spectra of human glioblastoma cell line U87 were recorded at different laser powers ranging from approximately 10 mW to a maximum of 107 mW, using a 63x water immersion objective with a numerical aperture of 0.90. The laser powers were determined using a 50x dry objective. The absolute intensity of the peak at 1440 cm^{-1} showed a linear increase with increasing power levels. Note that any significant detector background that will not scale with the laser power like thermal dark current and readout should be subtracted. A similar linear trend was observed for the peak at 1003 cm^{-1} (data not shown). In contrast, the ratio of these two peaks remained practically constant while increasing the laser power. Thus, when we are dealing with instrumental factors that have a linear influence on the peak intensities and that are often difficult to avoid or to correct for, the ratios of peaks are relatively unaffected.

(B) Background effects:

There can be a number of contributing factors leading to background variations in a spectrum, be it IR or Raman.

1) ***Sample effects***:

At times, the sample itself can be responsible for a strong background. Fluorescence is often a major problem in Raman spectroscopy, especially for biological specimens which are auto-fluorescent. Amino acids such as tyrosine, tryptophan and phenylalanine, organelles like lysosomes and chloroplasts and biomolecules like NADPH are strong contributors towards fluorescence in the near-UV and visible range[30]. This problem has been reduced by the use of near IR lasers like 785 nm and 830 nm[28]. Any remaining fluorescence that contributes to the baseline can be removed by background subtraction, although the shot noise of the background will still be present.

Apart from this, water can also be major reason for background fluctuations, especially in IR spectroscopy. Water being a strong IR absorber can reduce the signal intensity and thus affect the signal-to-noise ratio of an IR spectrum. This dictates the use of very thin and/or dehydrated samples for IR analysis. The residual water after dehydration and the atmospheric water vapour may contribute significantly in the 1600 cm^{-1} - 1750 cm^{-1} range and above 3000 cm^{-1}, requiring water vapour correction and smoothing of the spectrum[31]. Mie scattering can also result in background variations in an IR spectrum[32, 33].

Water is a weak Raman scatterer and hence does not preclude the analysis of biological samples by Raman spectroscopy under physiological conditions. However, for quantitative analysis subtraction of the water background becomes essential. If not performed, it can result in wrong spectral interpretations as illustrated in Figure 3. Raman spectra of a U87 cell line in Phosphate Buffered Saline (PBS) were recorded at 785 nm under a 63x water immersion objective with a numerical aperture of 0.90. The ratio of the peaks at 1440 and 1660cm^{-1} was calculated before and after background subtraction. Water has a broad Raman band at ~ 1630 cm^{-1} and contributes to the intensity of the broad Amide I peak at 1660 cm^{-1}. A clear difference in the ratio is observed due to the interference from the aqueous buffer. Background subtraction becomes important when peaks in the same wavenumber region are considered for ratioing, despite water being a weak Raman scatterer.

2) Substrate effects:

Glass and quartz which are regular substrates in optical and fluorescence microscopy are not well suited for IR or Raman microspectroscopy[34]. They are not transparent in the IR region and add a significant background to the Raman spectra, thereby reducing the signal to background ratio dramatically. Despite this fact, there are articles which have employed glass and quartz in Raman studies[10, 35]. Raman spectroscopy for biological samples is routinely done using calcium fluoride or magnesium fluoride windows. However, these have a strong background around 1200-1300 cm^{-1}. These substrates may not have a uniform effect on all parts of the sample: a thin region of the sample will have a stronger background contribution from the substrate than thick regions.

In case of transflection mode in IR spectroscopy, standing waves in the substrate can cause baseline undulations in the spectrum between 800 cm^{-1} to 1400 cm^{-1} which requires proper correction. Detailed accounts on the origin and correction methods are given by Filik *et al.*[36] and Bassan *et al.*[37] Ratiometric analysis of nearby peaks can also serve as one of the solutions to circumvent this problem.

The background contribution may also show wavelength dependence. This can be observed in Figure 4, which shows Raman spectra of *E. coli* plasmid DNA pKD4 recorded at 633 nm and 785 nm using a 50x objective with a numerical aperture of 0.75. Without baseline correction the 633-nm excited spectra show a strong, broad background, presumably from sample fluorescence and substrate (see Fig. 4(ii)). The bar graphs in Figure 4 (iii) and (iv) show that calculating the ratio of peaks that are close to each other like 1480 and 1580 cm^{-1} is less affected by background variations than the ratio of distant peaks such as 785 and 1580 cm^{-1}. The comparison of ratios from baseline corrected and un-corrected spectra shows less variation for proximate peaks than for distant peaks. Therefore, ratios can to some extent circumvent the effects of background fluctuations. Figure 4 (v) and (vi) depict the ratios calculated with the peak area approach. The background effects are better negated by the area method than by the intensity based method. However, the peaks and the method for ratioing have to be selected carefully. In the next section various ratioing techniques will be discussed in detail. After background correction a big difference in ratios remains between 785 and 633 nm excitation, mostly due to lower CCD sensitivity in the NIR, the factor $v_0(v_0 - v)^3$ in the Raman intensity, and

perhaps also the grating efficiency. These factors should also be corrected for when we want to compare ratios determined at different excitation wavelengths[28].

(C) Effect of uneven thickness:

Variations in sample thickness are inevitable even with careful sample preparation. However, a simple approach of taking peak ratios can reduce these effects to a significant degree. This point is illustrated in Figure 5.

Raman spectra of a dried droplet of a 0.3 mg/ml solution of Bovine Serum Albumin (BSA) were recorded at 633 nm using a 100x objective with a numerical aperture of 0.85. A Raman line map was obtained across the sample using the peak intensity at 1003 cm^{-1}. The mapped image (see Fig. 5(ii)) shows significant fluctuations in intensity across the sample due to thickness variation; similar trends were observed for a line map at 1660 cm^{-1} (not shown). The thickness variation in the dried sample droplet occurred as a result of the so-called coffee ring effect[38, 39]. Subsequently, a Raman line map was created using the peak intensity ratio of the 1003 and 1660 cm^{-1} bands. Figures 5 (iii) and (iv) clearly show that the ratio of these peak intensities did not change much across the rim of the "coffee ring". This demonstrates that peak ratios are much less affected by thickness variations in comparison with absolute intensities. Note, however, that ratioing low-intensity signals (the spectroscopic equivalent to dividing by zero) may lead to erratic results, as observed for the upper-left corner below 15 μm, i.e., outside the droplet. This is particularly evident from the calculated standard deviation for the region between 0-30 μm of the droplet, which is significantly higher than that for the region between 30-100 μm (see Fig. 5(v)). One should therefore be cautious when ratioing low intensity signals in image analysis.

Approaches for Ratio Analysis:

The benefits of ratiometric analysis are numerous but one must also know the various approaches used for such analyses and some of these will be discussed below. In Figure 6 the raw FTIR and Raman spectra of BSA are shown in frames (i) and (ii) respectively. Frame (iii) shows the various approaches used for intensity determination for ratiometric analysis with the Amide I band of the IR spectrum as an example.

1) Absolute intensity based methods:

This is a very common technique to calculate ratios in vibrational spectroscopy. The peak centres are determined and the intensities (peak heights) at those centres are used for ratio calculation. It is one of the easiest methods of ratiometric analysis for strong peaks with a good signal-to-noise ratio (Fig 6(iii) a). Although very simple to use, it does come with certain drawbacks. Baseline fluctuations can also affect this technique of ratiometric analysis. In order to avoid this, peak specific baseline corrections can be used to estimate the net intensity (see Table 1). This approach is less suitable when the spectrum suffers from a poor signal-to-noise ratio. Under such circumstances, it becomes very difficult to determine the exact peak centre and the intensity will suffer strongly from random fluctuations. Determining the peak maximum is also difficult when the peaks are broad. To circumvent these problems, other methods can be used.

2) Area based methods:

This approach uses the integrated area under a peak to determine ratios (Fig 6(iii), b). Although it is not as easy to apply as the absolute peak intensity based method, it can be used when spectra have a poor signal-to-noise ratio. Since more data points contribute to the total area the variability is reduced in comparison to the maximum intensity measurement. It is also a recommended technique in case of changing or fluctuating band widths or if the peaks are too narrow for the instrumental resolution. Similar to the absolute intensity based method; this method is also affected by baseline variations. Using a peak specific baseline correction can solve this issue (see Table 1). One of the shortcomings of this method is that it cannot be used in the case of broad peaks that result from the convolution of two or more peaks. This necessitates the use of deconvolution methods for calculating ratios, as will be discussed below.

3) Curve fitted area based methods:

Often vibrational spectra have broad peaks such as the Amide I band. Intensity and area based ratiometric analysis of such broad peaks may result in an inaccurate interpretation, especially if adjacent peaks contribute to the peak area. The solution is offered by curve fitted area based methods after peak deconvolution (see Fig 6(iv)). The method employs the use of the 2nd derivative of the spectrum to find the number of peaks in the broad band as well as

their centres. Sometimes a broad band can be also be fitted with a single peak and the area and the peak centre can be deduced (see Fig 6(iii) c).

Figure 6 compares the ratio of the 1657/1545 bands calculated using the different methods in an FTIR spectrum (v) and the ratio of the 1448/1654 bands determined using the various methods in a Raman spectrum (vi). We observe that there are variations in the ratio calculated with these methods. This is due to the fact that each approach takes values for ratioing differently and may be affected differently by overlapping peaks. It is generally better to adopt one single technique when comparing different groups of data.

The Raman spectrum of a 10 mg/ml dried droplet of BSA was recorded under a 100x objective with a numerical aperture of 0.85 using a 633 nm laser. The spectrum was recorded from 700-1700 cm^{-1} and in Fig. 6(iv) the range from 1220 to 1380 cm^{-1} is shown on an expanded wavenumber scale. Four peaks were fitted with centres at 1247, 1271, 1316 and 1338 cm^{-1} respectively as deduced by the 2nd derivative approach.

In Figure 7, the FTIR spectrum of a dehydrated droplet of 0.3 mg/ml Bovine serum albumin (BSA) was recorded using a 15x Cassegrain objective. Although the spectrum was recorded from 900-3500 cm^{-1}, here only the range from 1060-1140 cm^{-1} is shown. Peak fitting was done using Origin 8.5 software. Three peaks were fitted with centres at 1081, 1109 and 1125 cm^{-1} respectively, as determined by the 2nd derivative method. The intensities at these peak centres were then used to determine the ratio of the 1081/1125 bands. A comparison was made with the absolute intensity based method for ratiometric analysis (without curve fitting). The bar graph (Figure 7, (ii)) shows the difference between the ratios observed for the two methods. The apparent increase in intensity observed for the 1125 cm^{-1} peak in the raw spectrum is due to the convolution of the bands at 1109 cm^{-1} and 1125 cm^{-1}, which leads to a decrease in the ratio of 1081/1125. This decrease is not due to a change in relative biochemical composition. A similar approach has been employed by Petibois *et al.*[40]

The advantages of ratiometric analysis in spectroscopy are plenty. However, the methods used for calculating such ratios should be selected carefully. It is at the researchers' discretion to adopt the appropriate method for their study. Table 1 summarizes the approaches used for determining peak ratios along with their advantages and disadvantages.

Apart from the approaches mentioned above, other related techniques have also been used for ratiometric analysis. A sum or difference of two peak intensities can also be considered for obtaining ratios[41, 42]. To be precise, let X, Y, Z represent intensities at three different wavenumbers. The Sum and the difference are explained as follows. (i) Sum of Intensities: If the band wavenumbers that correspond to X and Y are of the same molecular origin, then the sum of X+Y can be ratioed with Z. (ii) Difference of Intensities: Instead of taking a ratio of X/Z directly, Y is subtracted from both X and Z ((X-Y)/ (Z-Y)), where Y is situated in close proximity to both X and Z. This method was employed by the authors to circumvent background contribution.

The practice of ratiometric analysis circumvents variations associated with sample thickness, background fluctuations and other instrumental effects. Additionally, it can also be used to determine the contributions of individual biochemical components within a sample. For example, the peak at 1440 cm^{-1} has been assigned to CH_2 bending, which has contributions from both lipids and proteins. In order to determine the component getting predominantly modulated upon any change in this band, the ratio between the bands at 1440 and 1003 is an excellent indicator. This is because the band at 1003 cm^{-1} has contributions only from phenylalanine present in proteins. As a result, taking the ratio between the 1440 and 1003 cm^{-1} bands will nullify the protein contribution and give information about the composition of lipids. Thus, individual biochemical components can be quantified, which is relevant for clinical investigations.

In Raman spectroscopy, the intensity ratio between the perpendicular and parallel component of scattered light is known as the depolarisation ratio. It is denoted by ρ:

$$\rho = I_{perpendicular}/I_{parallel}$$

Conventionally, these ratios have been used for symmetry analysis of compounds[43, 44]. A unique application of the depolarisation ratio has been demonstrated by some groups for clinical investigations. Depolarisation ratios can be used to predict or determine the status of dental hygiene. In a study, depolarisation ratios for the band at 959 cm^{-1} (assigned to hydroxyapatite phosphate) were compared between healthy and carious sites in 23 extracted human teeth. The reduction in depolarisation ratio was found to be higher for normal enamel compared to carious enamel. Thus, depolarisation ratios can serve as an indicator for biochemical and structural changes occurring within enamel as a result of demineralisation.

In another study, the Amide I depolarisation ratio was used to determine the structure of lens crystallin proteins in excised bovine eye lenses. It was determined that these lens proteins were organised in anti-parallel, pleated β-sheet structures[45].

Effects of pre-processing on ratio:

Preprocessing is an important step in the analysis of any vibrational spectrum. Many pre-processing methods are routinely used[4, 46]. These include baseline correction, smoothing and normalisation. Since ratiometric analysis is itself a normalisation method for a peak, complete spectral normalisation does not affect ratioing. However, baseline correction does have an effect. This effect becomes pronounced in the case of peaks that are differently affected by baseline fluctuations, for example the distant peaks of the spectra in Figure 4. It is judicious to perform a peak specific baseline correction in order to avoid baseline effects on ratiometric analysis.

Noise in the spectra can originate from various sources. For example, in IR spectroscopy, substrate, water, etc can reduce the measured intensity and thus contribute to the noise in the spectrum. In case of Raman spectroscopy thermal noise of the detector, low power, low scattering and Charge Coupled Device (CCD) efficiency for higher wavelengths (785 nm, 830 nm etc) may lead to a lower Signal Noise ratio (SNR) [28].Furthermore, it is evident from Figure 5 that the edges of the ratio plot have lower SNR than the middle region. This is due to ratioing weak signal. This reduction of SNR can be avoided by not taking ratios between weak signals in Raman, whereas it is unavoidable in IR spectroscopy. Absorbance measured in IR spectroscopy is a logarithmic ratio between transmitted and incident intensity. A common solution to improve SNR is smoothing the data.

Another major contribution towards noise in Raman spectroscopy is from cosmic rays. These are generated due to high-energy particle passage through the CCD, causing generation of electrons, which the CCD interprets as signal. These rays are totally random, appear as very sharp emission lines and usually affect only one pixel at a time. Thus, all Raman spectra should also be corrected for cosmic rays before further pre-processing is performed[6].

Smoothing becomes particularly important when ratios are calculated after spectral deconvolution. An important point to be taken into account is the need for a correct smoothing procedure when a deconvolution method is used. Improper smoothing of the second derivative can result in either overestimation or underestimation of peaks hidden in the broad band. A comparative analysis of pre-processing effects on various ratioing methods is given in Table 1. The selection of the appropriate pre-processing approach depends on the spectral quality which is governed by sample, substrate, and instrumental parameters. While it is at the user's discretion to use pre-processing methods, it should not result in erroneous interpretation. For example, during baseline correction using polynomial fitting method, care should be taken that no new peaks are created and no alteration between the ratios of nearby peaks occur. For further information on pre-processing methods kindly refer to Kelly J G *et al.*, Popp *et al.*, Gautam *et al.*[4, 46, 47].

Statistical analysis of ratios:

Once the ratios have been determined, it is important to deduce whether the ratios of the groups being compared are significantly different or not. Often one needs to resort to statistical tools in order to accomplish this. Several inferential statistical tools can be employed for this purpose. A few commonly used statistical tests include the Student's t-test[27, 48], one-way or two-way ANOVA tests[49, 50], Mann Whitney test[49, 51] etc. These statistical tests play an important role in defining threshold values for ratios that can be translated into a clinical parameter. We have performed statistical analysis using Student's t-test on the data of Figure 3 and Figure 5. Furthermore, multivariate analysis like K means clustering has been applied on a collection of ratios to detect liver tumors.[52]

RATIOMETRIC IMAGING

Ratios can also be used to create IR and Raman images. These can reveal the distribution of various biochemical components that are of clinical significance, such as proteins, lipids, carbohydrates and nucleic acids across cells and tissues under various conditions. Figures 8 and 9 illustrate how ratios can be used to map images of tissues. Care has been taken as regards proper scaling of the colour codes in IR and Raman images as mentioned by Ashton *et al.*[53] This is an essential step in any image analysis. It is evident from the ratioing of

images that artefacts like thickness variations are cancelled out resulting in analysis of true biochemical changes, which is of more relevance for clinical analysis.

In order to demonstrate IR mapping images using ratios, a 4 μm thick section of mouse kidney tissue was used and FTIR spectra were recorded using a multichannel 64x64 Focal Plane Array (FPA) detector. Figure 8 (i) shows the bright field image of the tissue; (ii) shows IR images mapped using the absolute intensity at 1537 and 1650 cm^{-1} and the ratio image of 1537/1650. A similar mapping was done using the peak area ratio method, although for this sample the images based on peak intensity ratios or peak area ratios did not show any major differences. The scales of IR intensity, ratio and PCA maps were kept between 0 and 1 (A.U.) whereas the area was scaled from 0 to 30 arbitrary units (A.U.)

A multivariate approach can also be used for creation of an IR image. Figure 8(iii) shows the Principal Component Analysis (PCA) image of the tissue. This method uses the entire spectrum for mapping the IR image. However, clinicians may prefer to investigate the distribution of a single or a group of relevant biochemical components under diseased conditions. Therefore, univariate approaches might suit a clinical setting better than multivariate approaches.

Similarly, Raman images can also be created using ratiometric analysis. This is illustrated in Figure 9 for a 10 μm thick mouse kidney section. Raman spectra were recorded for the selected region of the tissue using a 785 nm laser under a 50x objective with a numerical aperture of 0.75.

Figure 9 (i) shows the bright field image of the kidney section and (ii) shows Raman images mapped using area intensity at 1440 cm^{-1} and at 1660 cm^{-1}, along with a Raman image created using the ratio of the 1440/1660 cm^{-1} bands. The scales were adjusted between 0 and 300000 A.U. for the area maps and from 0 to 1 A.U. for the ratio map.

Although for this relatively homogeneous section the ratio map doesn't show any variations across the sample, it nullifies the effect of variations in thickness across the section. When used for monitoring disease prognosis, however, as shown by Gautam *et al.* for studying sepsis induced by *Salmonella typhimurium*, the ratio facilitates for the heterogeneity analysis of biomolecules across various time point[27]. Thus, ratio maps are of significant importance in

experiments that involve scenarios like time dependent or concentration dependent monitoring of changes across various samples.

LIBRARY OF RATIOS IN IR AND RAMAN SPECTROSCOPY

Several biological phenomena have been studied using ratiometric analysis, including the detection of drug-induced changes in tissues[48], detection of diabetes[54], classification of premalignant and malignant stages of cancer[55, 56], classification of brain tissues representing different stages of tumour[57, 58], depiction of mineralisation in tissues[59], quantification of damage in nuclear DNA[60], estimation of post-mortem interval and monitoring the biochemical changes that occur post-mortem[61], identification of bacteria[62, 63], identification of different types of cataract lens abnormalities[14], liver injury[48], and the effects of oxidative stress or radical aggregation in tissues[64]. These and other ratiometric studies have been summarised in Table 2 for IR and in Table 3 for Raman spectra. In both tables the entries are listed according to the wavenumbers of the respective bands. The biomolecular origin of the peaks listed in the ratios was mostly adopted from the cited papers, otherwise we have used the assignments from Movasaghi *et al.* for both IR[7] and Raman[65] peaks In case of discrepancies, the assignments have been mentioned as "assignment unclear". In Table 2 and 3, all ratios have been calculated using the peak intensity based method unless otherwise mentioned as peak area based or curve fitted area based.

(a) Infra-red ratios:

Towards the very end of the twentieth century, Wong *et al.* used IR spectroscopy to describe the structural changes occurring inside human cervical cells during cancer. Using the intensity ratio of two peaks, they were able to differentiate between normal and malignant tissues[55]. The cytoplasm-to-nucleus ratio, one of the important hallmarks of cancer, was directly correlated to the Amide II/ phosphate stretching ratio; this was in agreement with the fact that protein is predominant in cytoplasm[55]. Since then, over the past two decades IR ratiometric analysis has been used extensively to differentiate between cancerous and noncancerous tissues. Moreover, grading of various cancer stages has also been done. Benedetti *et al.* have quantified relative levels of nucleic acids and proteins by calculating binary ratios such as DNA/RNA, DNA/protein, RNA/protein and ternary ratios like DNA/RNA/protein[66]. In general, multivariate analysis is employed to obtain information about the entire spectrum, but recently Zhaomin Chen *et al.* have considered 64 IR intensity

and area ratios (e.g. (1144-1182)/1544, 1012/1256, 1016/1080, 1024/1080, 1024/1080, 1084/1244, 1080/1244, 1050/1034, 1120/1020, 2924/1544, 1080/1548 etc.) and employed 20 of them for multivariate analysis (K- means cluster analysis) to diagnose liver cancer[52]. Furthermore, the ratio of protein to lipid and protein to glycogen is used for differentiating the growth stages in mammalian cell cultures[26]. Table 2 gives a non-exhaustive overview of various IR ratios reported in the literature.

Several researchers have reported standard values of ratios for disease detection. For example, Chang *et al.* has reported that the area ratio of the 1155/1240 peaks is 1.40±0.91 for normal human cervical tissues and 0.29±0.19 for cancerous tissues[67]. The condition of the eye lens was also linked to various ratio values by Lin *et al*[14] The Amide I/ Amide II ratio is set to be 2.20-2.33 for normal lenses, 1.28-1.41 for immature cataractous lens and 1.04-1.13 for glaucomatous lens. Another parameter evaluated by the same authors is the 2965/2930 ratio value for similar analysis. Normal lens: 0.702, premature cataractous lens: 0.382, glaucomatous lens: 0.377. Krafft *et al.* have given specifications for three 'molecular descriptors' for the detection of malignant glyomas in different stages[41]. The 2850/1655 ratio value was found to be >0.5 for normal tissue, 0.3 for astrocytoma second degree, 0.2 for astrocytoma third degree and 0.1 for Glioblastoma. For haemorrhage and leptomenings the ratio was found to be 0.08 and 0.16 respectively. For haemorrhage the 1545/1656 ratio increases from 0.6 to more than 0.67. The ratio value of (1231+1450)/1655 maintains in the range of 0.22 to 0.88 for leptomenings[41].

(b) Raman ratios:

The Raman ratios used for biomedical analysis are listed in Table 3. Short *et al.* used combinations of pure component spectra of biomolecules to fit the spectra of cells and deduced protein/lipid, protein/RNA, Protein/ DNA, lipid/ RNA, lipid/DNA and RNA/ DNA ratios to understand cell proliferation[68]. Taleb *et al.* employed LDA (Linear Discriminant Analysis), a multivariate analysis tool, to analyse 5 different adjacent band ratios (ABR) and differentiated PNT1A (immortalised normal prostate cell line) from LNCaP (malignant cell line derived from prostate metastases)[69]. Nyman and co-workers have given an extensive review on all the ratios used to analyse the composition of bones by Raman spectroscopy[59]. They have summarised Raman ratios that are used to estimate carbonates, phosphates, the

extent of mineralisation and various other pathological states of bone. The biochemical components of human hair were quantified based on the signal enhancement by ratiometric analysis using Coherent Antistokes Raman Scattering microscopy (CARS)[70], a fast mapping technique that requires the use of two synchronized picosecond pulsed lasers[71-73].

Bhushan *et al.* have reported that the 1441/1652 ratio value for normal breast tissue is 1.65 ± 0.22 while that for abnormal tissues is 0.65±0.35[74]. Another parameter proposed by them is the 1452/1600 ratio value, which is 1.33 ± 0.34 and 1.41±0.39 for normal and abnormal tissues, respectively. Gniadecka *et al*. have shown different values for normal cells and basal carcinomic cells for the (1290–1360) / (1230–1290) area ratio: 0.29 (0.22–0.36) for normal and 1.37 (1.21–1.54) for carcinogenic cells[75]. Huang *et al*. have stated a boundary for detection of liver cancer for several ratio values by SERS. (937/1209 =1.462; 1276/1308 = 1.234; 1342/1375 = 1.515; 1402/1435 = 1.618)[76]. The sensitivity and specificity was found to be about 90% for each case[76]. Chen *et al*. have also proposed some parameters with values to detect cancer in the case of gastric mucosa: the 1585/853 ratio value is 0.90±0.74 for cancerous sample and 0.42±0.29 for normal sample with p value 0.03, accuracy 73.3% sensitivity 67% and specificity 80%[77]. Huang *et al.* have demonstrated different 656/725 ratio values for normal and cancerous sample (0.409±0.0.082 for normal and 0.900±0.362 for cancerous sample), using a SERS based Raman spectroscopic method[78]. Huang *et al.* have found the 1449/1418 ratio value to be 1.13±0.05 for people having normal seminal plasma and 1.26±0.15 for abnormal groups (unpaired student's t-test, $P < 0.05$)[79]. Although the first ratio value is an indicative signature value of DNA damage due to induced stress, the second ratio value here does not support that hypothesis[79]. Sokolov *et al*. have mentioned the 1360/ 1340 ratio in UV visible resonance Raman Spectroscopy for different types of sickle cell haemoglobin fibers as 2.7, 2.5, 2.2, 2.6, 2.1, and 2.2 for fibers, T state, R state, T-R state, F-R state and F-T state respectively[80].

CONCLUSION

For a technique to evolve as a diagnostic tool in the field of medicine either the limitations of the existing techniques have to be surmounted or it must be able to provide novel information. Vibrational spectroscopy with advanced spectral analysis not only has the strength for equating with the pathologist but also has the potential to become a tool for the relative quantification of biomolecules by determining ratios that can act as markers for disease diagnosis or treatment prognosis. These parameters do not demand strong

computational skills and can be of great use in Point-of-Care (POC) devices where rapidity along with sensitivity and specificity is crucial.

Acknowledgments:

We thank the Department of Science and Technology (DST) and Department of Biotechnology (DBT), Government of India, for financial support. SU acknowledges the J.C. Bose Fellowship from DST. SK thanks DST for INSPIRE fellowship. TV and RM thank IISc and CSIR for research fellowships respectively.

References

1. B. Singh, R. Gautam, S. Kumar, B. N. V. Kumar, U. Nongthomba, D. Nandi, G. Mukherjee, V. Santosh, K. Somasundaram and S. Umapathy, *Curr Sci India*, 2012, 102, 232-244.
2. R. Gautam, A. Samuel, S. Sil, D. Chaturvedi, A. Dutta, F. Ariese and S. Umapathy, *Curr Sci India*, 2015, 108, 341-356.
3. M. J. Baker, J. Trevisan, P. Bassan, R. Bhargava, H. J. Butler, K. M. Dorling, P. R. Fielden, S. W. Fogarty, N. J. Fullwood, K. A. Heys, C. Hughes, P. Lasch, P. L. Martin-Hirsch, B. Obinaju, G. D. Sockalingum, J. Sule-Suso, R. J. Strong, M. J. Walsh, B. R. Wood, P. Gardner and F. L. Martin, *Nat Protoc*, 2014, 9, 1771-1791.
4. T. Bocklitz, A. Walter, K. Hartmann, P. Rosch and J. Popp, *Anal Chim Acta*, 2011, 704, 47-56.
5. S. Pahlow, S. Meisel, D. Cialla-May, K. Weber, P. Rosch and J. Popp, *Adv Drug Deliv Rev*, 2015, DOI: 10.1016/j.addr.2015.04.006.
6. R. Gautam, Ph.D., Indian Institute of Science, 2014.
7. Z. Movasaghi, S. Rehman and I. U. Rehman, *Appl Spectrosc Rev*, 2008, 43, 134-179.
8. A. C. S. Talari, Z. Movasaghi, S. Rehman and I. U. Rehman, *Appl Spectrosc Rev*, 2015, 50, 46-111.
9. H. J. Byrne, M. Baranska, G. J. Puppels, N. Stone, B. Wood, K. M. Gough, P. Lasch, P. Heraud, J. Sule-Suso and G. D. Sockalingum, *Analyst*, 2015, 140, 2066-2073.
10. A. F. Palonpon, J. Ando, H. Yamakoshi, K. Dodo, M. Sodeoka, S. Kawata and K. Fujita, *Nat Protoc*, 2013, 8, 677-692.
11. S. A. Oladepo, K. Xiong, Z. Hong, S. A. Asher, J. Handen and I. K. Lednev, *Chem Rev*, 2012, 112, 2604-2628.
12. J. Popp, C. Krafft and T. Mayerhöfer, *Optik & Photonik*, 2011, 6, 24-28.
13. F. M. Lyng, I. R. M. Ramos, O. Ibrahim and H. J. Byrne, *Appl Sci* 2015, 5, 23-35.
14. S. Y. Lin, M. J. Li and W. T. Cheng, *Spectrosc-Int J*, 2007, 21, 1-30.
15. R. A. Shaw and H. H. Mantsch, *Encyclopedia of Analytical Chemistry*, John Wiley & Sons, New York, 2001.
16. A. Gaw, J. M. Murphy, A. R. Cowan, J. M. Stewart and J. Shepherd, *Clinical Biochemistry*, Elsevier, United Kingdom, 2005.
17. D. Sebiskveradze, V. Vrabie, C. Gobinet, A. Durlach, P. Bernard, E. Ly, M. Manfait, P. Jeannesson and O. Piot, *Lab Invest*, 2011, 91, 799-811.
18. M. N. Gurcan, L. E. Boucheron, A. Can, A. Madabhushi, N. M. Rajpoot and B. Yener, *IEEE Rev Biomed Eng*, 2009, 2, 147-171.
19. A. Banas, K. Banas, A. Furgal-Borzych, W. M. Kwiatek, B. Pawlicki and M. B. Breese, *Analyst*, 2015, 140, 2156-2163.

20. M. Fung Kee Fung, M. Senterman, P. Eid, W. Faught, N. Z. Mikhael and P. T. Wong, *Gynecol Oncol*, 1997, 66, 10-15.
21. U. Utzinger, D. L. Heintzelman, A. Mahadevan-Jansen, A. Malpica, M. Follen and R. Richards-Kortum, *Appl Spectrosc*, 2001, 55, 955-959.
22. A. Nijssen, T. C. B. Schut, F. Heule, P. J. Caspers, D. P. Hayes, M. H. A. Neumann and G. J. Puppels, *J Invest Dermatol*, 2002, 119, 64-69.
23. U. Neugebauer, S. Trenkmann, T. Bocklitz, D. Schmerler, M. Kiehntopf and J. Popp, *J Biophotonics*, 2014, 7, 232-240.
24. J. Trevisan, P. P. Angelov, P. L. Carmichael, A. D. Scott and F. L. Martin, *Analyst*, 2012, 137, 3202-3215.
25. F. Bonnier and H. J. Byrne, *Analyst*, 2012, 137, 322-332.
26. J. R. Mourant, Y. R. Yamada, S. Carpenter, L. R. Dominique and J. P. Freyer, *Biophys J*, 2003, 85, 1938-1947.
27. R. Gautam, M. Deobagkar-Lele, S. Majumdar, B. Chandrasekar, E. Victor, S. M. Ahmed, N. Wadhwa, T. Verma, S. Kumar, N. R. Sundaresan, S. Umapathy and D. Nandi, *J Biophotonics*, 2015, 9999.
28. R. L. McCreery, *Raman Spectroscopy for Chemical Analysis*, Wiley-Interscience Publication, USA, 2001.
29. R. P. Griffiths and J. A. de Haseth, *Fourier Transform Infrared Spectrometry*, John Wiley and Sons, New Jersey, 2007.
30. M. Monici, *Biotechnol Annu Rev*, 2005, 11, 227-256.
31. D. Perez-Guaita, J. Kuligowski, G. Quintas, S. Garrigues and M. de la Guardia, *Appl Spectrosc*, 2013, 67, 1339-1342.
32. B. Mohlenhoff, M. Romeo, M. Diem and B. R. Wood, *Biophys J*, 2005, 88, 3635-3640.
33. P. Bassan, A. Sachdeva, A. Kohler, C. Hughes, A. Henderson, J. Boyle, J. H. Shanks, M. Brown, N. W. Clarke and P. Gardner, *Analyst*, 2012, 137, 1370-1377.
34. A. G. Shen, Y. Ye, J. W. Zhang, X. H. Wang, J. M. Hu, W. Xie and J. Shen, *Vib Spectrosc*, 2005, 37, 225-231.
35. L. T. Kerr, H. J. Byrne and B. M. Hennelly, *Anal Methods-Uk*, 2015, 7, 5041-5052.
36. J. Filik, M. D. Frogley, J. K. Pijanka, K. Wehbe and G. Cinque, *Analyst*, 2012, 137, 853-861.
37. P. Bassan, J. Lee, A. Sachdeva, J. Pissardini, K. M. Dorling, J. S. Fletcher, A. Henderson and P. Gardner, *Analyst*, 2013, 138, 144-157.
38. T. S. Wong, T. H. Chen, X. Y. Shen and C. M. Ho, *Anal Chem*, 2011, 83, 1871-1873.
39. R. D. Deegan, O. Bakajin, T. F. Dupont, G. Huber, S. R. Nagel and T. A. Witten, *Nature*, 1997, 389, 827-829.
40. C. Petibois and G. Deleris, *Trends Biotechnol*, 2006, 24, 455-462.
41. C. Krafft, K. Thummler, S. B. Sobottka, G. Schackert and R. Salzer, *Biopolymers*, 2006, 82, 301-305.
42. P. G. Andrus and R. D. Strickland, *Biospectroscopy*, 1998, 4, 37-46.
43. D. P. Strommen, *J Chem Educ*, 1992, 69, 803-807.
44. P. A. Terpstra, C. Otto, G. M. J. Segersnolten, J. S. Kanger and J. Greve, *Biospectroscopy*, 1995, 1, 255-263.
45. M. D. Morris, *Emerging Raman Applications and Techniques in Biomedical and Pharmaceutical Fields*, Springer, London, 2010.
46. J. G. Kelly, J. Trevisan, A. D. Scott, P. L. Carmichael, H. M. Pollock, P. L. Martin-Hirsch and F. L. Martin, *J Proteome Res*, 2011, 10, 1437-1448.

47. R. Gautam, S. Vanga, F. Ariese and S. Umapathy, *EPJ Techniques and Instrumentation*, 2015, 2.
48. R. Gautam, B. Chandrasekar, M. Deobagkar-Lele, S. Rakshit, B. N. V. Kumar, S. Umapathy and D. Nandi, *Plos One*, 2012, 7, e45521.
49. D. Farlay, M. E. Duclos, E. Gineyts, C. Bertholon, S. Viguet-Carrin, J. Nallala, G. D. Sockalingum, D. Bertrand, T. Roger, D. J. Hartmann, R. Chapurlat and G. Boivin, *Plos One*, 2011, 6, e28736.
50. S. Luo, C. Chen, H. Mao and S. Jin, *J Biomed Opt*, 2013, 18, 067004.
51. A. Dogan, K. Ergen, F. Budak and F. Severcan, *Appl Spectrosc*, 2007, 61, 199-203.
52. Z. Chen, R. Butke, B. Miller, C. L. Hitchcock, H. C. Allen, S. P. Povoski, E. W. Martin, Jr. and J. V. Coe, *J Phys Chem B*, 2013, 117, 12442-12450.
53. L. Ashton, K. A. Hollywood and R. Goodacre, *Analyst*, 2015, 140, 1852-1858.
54. O. Bozkurt, M. Severcan and F. Severcan, *Analyst*, 2010, 135, 3110-3119.
55. P. T. T. Wong, R. K. Wong, T. A. Caputo, T. A. Godwin and B. Rigas, *P Natl Acad Sci USA*, 1991, 88, 10988-10992.
56. Y. Yazdi, N. Ramanujam, R. Lotan, M. F. Mitchell, W. Hittelman and R. Richards-Kortum, *Appl Spectrosc*, 1999, 53, 82-85.
57. B. Singh, Ph.D Indian Institute of Science, 2012.
58. Y. Zhou, C. H. Liu, Y. Sun, Y. Pu, S. Boydston-White, Y. L. Liu and R. R. Alfano, *J Biomed Opt*, 2012, 17.
59. J. S. Nyman, A. J. Makowski, C. A. Patil, T. P. Masui, E. C. O'Quinn, X. H. Bi, S. A. Guelcher, D. P. Nicollela and A. Mahadevan-Jansen, *Calcified Tissue Int*, 2011, 89, 111-122.
60. V. Sanchez, K. Redmann, J. Wistuba, F. Wubbeling, M. Burger, H. Oldenhof, W. F. Wolkers, S. Kliesch, S. Schlatt and C. Mallidis, *Fertil Steril*, 2012, 98, 1124-+.
61. Y. Tuo, P. Huang, Y. Ke, S. L. Fan, Q. Y. Lu, B. Xin and Z. Y. Wang, *Appl Spectrosc*, 2010, 64, 268-274.
62. H. X. Tian, G. Q. Zhuang, A. Z. Ma and C. Y. Jing, *J Microbiol Meth*, 2012, 89, 153-158.
63. Q. Wu, T. Hamilton, W. H. Nelson, S. Elliott, J. F. Sperry and M. Wu, *Anal Chem*, 2001, 73, 3432-3440.
64. J. Y. Li, G. G. Ying, K. C. Jones and F. L. Martin, *Analyst*, 2015, 140, 2687-2695.
65. Z. Movasaghi, S. Rehman and I. U. Rehman, *Appl Spectrosc Rev*, 2007, 42, 493-541.
66. E. Benedetti, E. Bramanti, F. Papineschi, I. Rossi and E. Benedetti, *Appl Spectrosc*, 1997, 51, 792-797.
67. J. I. Chang, Y. B. Huang, P. C. Wu, C. C. Chen, S. C. Huang and Y. H. Tsai, *Gynecologic Oncology*, 2003, 91, 577-583.
68. K. W. Short, S. Carpenter, J. P. Freyer and J. R. Mourant, *Biophys J*, 2005, 88, 4274-4288.
69. A. Taleb, J. Diamond, J. J. McGarvey, J. R. Beattie, C. Toland and P. W. Hamilton, *J Phys Chem B*, 2006, 110, 19625-19631.
70. M. Zimmerley, C. Y. Lin, D. C. Oertel, J. M. Marsh, J. L. Ward and E. O. Potma, *J Biomed Opt*, 2009, 14.
71. C. L. Evans, E. O. Potma, M. Puoris'haag, D. Cote, C. P. Lin and X. S. Xie, *P Natl Acad Sci USA*, 2005, 102, 16807-16812.
72. S. H. Parekh, Y. J. Lee, K. A. Aamer and M. T. Cicerone, *Biophys J*, 2010, 99, 2695-2704.
73. C. H. Camp and M. T. Cicerone, *Nat Photonics*, 2015, 9, 295-305.

74. B. Bhushan and A. Pradhan, *International Journal of Innovative Research in Science, Engineering and Technology*, 2013, 2.
75. M. Gniadecka, H. C. Wulf, N. N. Mortensen, O. F. Nielsen and D. H. Christensen, *J Raman Spectrosc*, 1997, 28, 125-129.
76. J. Huang, S. Liu, Z. Chen, N. Chen, F. Pang and T. Wang, *Technol Cancer Res Treat*, 2014, DOI: 10.1177/1533034614561358.
77. Y. Chen, J. H. Dai, X. Q. Zhou, Y. J. Liu, W. Zhang and G. Y. Peng, *Plos One*, 2014, 9.
78. Z. F. Huang, Z. F. Li, R. Chen, G. N. Chen, D. Lin, G. Q. Xi, Y. J. Chen, H. X. Lin and J. P. Lei, *J Phys Conf Ser*, 2011, 277.
79. Z. F. Huang, X. W. Chen, Y. P. Chen, J. H. Chen, M. Dou, S. Y. Feng, H. S. Zeng and R. Chen, *J Biomed Opt*, 2011, 16.
80. L. Sokolov and I. Mukerji, *J Phys Chem B*, 2000, 104, 10835-10843.
81. A. Podshyvalov, R. K. Sahu, S. Mark, K. Kantarovich, H. Guterman, J. Goldstein, R. Jagannathan, S. Argov and S. Mordechai, *Appl Optics*, 2005, 44, 3725-3734.
82. C. Conti, P. Ferraris, E. Giorgini, T. Pieramici, L. Possati, R. Rocchetti, C. Rubini, S. Sabbatini, G. Tosi, M. A. Mariggio and L. Lo Muzio, *J Mol Struct*, 2007, 834, 86-94.
83. P. Huang, W. P. Tian, Y. Tuo, Z. Y. Wang and G. D. Yang, *Spectrosc Lett*, 2009, 42, 108-116.
84. M. Baranska, ed., *Optical Spectroscopy and Computational Methods in Biology and Medicine.*, Springer, New York 2014.
85. P. Palaniappan, K. Pramod and V. Vijayasundaram, *J Appl Spectrosc*, 2008, 75, 752-758.
86. E. Bogomolny, S. Argov, S. Mordechai and M. Huleihel, *Bba-Gen Subjects*, 2008, 1780, 1038-1046.
87. S. Mordechai, R. K. Sahu, Z. Hammody, S. Mark, K. Kantarovich, H. Guterman, A. Podshyvalov, J. Goldstein and S. Argov, *J Microsc*, 2004, 215, 86-91.
88. L. Chiriboga, P. Xie, H. Yee, V. Vigorita, D. Zarou, D. Zakim and M. Diem, *Biospectroscopy*, 1998, 4, 47-53.
89. T. Gao, J. Feng and Y. Ci, *Anal Cell Pathol*, 1999, 18, 87-93.
90. D. C. Fernandez, R. Bhargava, S. M. Hewitt and I. W. Levin, *Nat Biotechnol*, 2005, 23, 469-474.
91. R. Eckel, H. Huo, H. W. Guan, X. Hu, X. Che and W. D. Huang, *Vib Spectrosc*, 2001, 27, 165-173.
92. A. M. Melin, A. Perromat and G. Deleris, *Can J Physiol Pharm*, 2001, 79, 158-165.
93. L. P. Choo, M. Jackson, W. C. Halliday and H. H. Mantsch, *Biochim Biophys Acta*, 1993, 1182, 333-337.
94. C. Petibois, B. Drogat, A. Bikfalvi, G. Deleris and M. Moenner, *FEBS Lett*, 2007, 581, 5469-5474.
95. C. Krafft, W. Hinrichs, P. Orth, W. Saenger and H. Welfle, *Biophys J*, 1998, 74, 63-71.
96. J. Y. Li, R. Strong, J. Trevisan, S. W. Fogarty, N. J. Fullwood, K. C. Jones and F. L. Martin, *Environ Sci Technol*, 2013, 47, 10005-10011.
97. N. Stone, Ph.D., Cranfield University, 2001.
98. L. Guerrini, Z. Krpetic, D. van Lierop, R. A. Alvarez-Puebla and D. Graham, *Angew Chem Int Edit*, 2015, 54, 1144-1148.
99. A. Bankapur, R. S. Krishnamurthy, E. Zachariah, C. Santhosh, B. Chougule, B. Praveen, M. Valiathan and D. Mathur, *Plos One*, 2012, 7.

100. A. Downes, R. Mouras, P. Bagnaninchi and A. Elfick, *J Raman Spectrosc*, 2011, 42, 1864-1870.
101. M. Pezolet, M. Pigeon-Gosselin, J. Nadeau and J. P. Caille, *Biophys J*, 1980, 31, 1-8.
102. Y. Liu, Y. Zhu and Z. Li, *Translational Andrology and Urology*, 2014, 3, 125-133.
103. C. Xie, J. Mace, M. A. Dinno, Y. Q. Li, W. Tang, R. J. Newton and P. J. Gemperline, *Anal Chem*, 2005, 77, 4390-4397.
104. S. Bernatova, O. Samek, Z. Pilat, M. Sery, J. Jezek, P. Jakl, M. Siler, V. Krzyzanek, P. Zemanek, V. Hola, M. Dvorackova and F. Ruzicka, *Molecules*, 2013, 18, 13188-13199.
105. C. Krafft, T. Knetschke, R. H. W. Funk and R. Salzer, *Anal Chem*, 2006, 78, 4424-4429.
106. G. Das, F. Mecarini, F. Gentile, F. De Angelis, H. Mohan Kumar, P. Candeloro, C. Liberale, G. Cuda and E. Di Fabrizio, *Biosens Bioelectron*, 2009, 24, 1693-1699.
107. S. K. Teh, W. Zheng, K. Y. Ho, M. Teh, K. G. Yeoh and Z. Huang, *Br J Cancer*, 2008, 98, 457-465.
108. R. Ihtesham ur, Zanyar Movasaghi, Shazza Rehman ed., *Vibrational Spectroscopy for Tissue Analysis*, CRC Press, Taylor and Francis Group, Florida, 2013.
109. M. Alebrahim, Ph.D., Friedrich-Schiller-Universität:, 2013.
110. D. B. Zohreh, H. M. B. Mohammad, K. Ehsanollah and M. Rasoul, *Iranian Journal of Medical Physics*, 2014, 11, 308-315.
111. Y. Hu, A. Shen, T. Jiang, Y. Ai and J. Hu, *Spectrochim Acta A Mol Biomol Spectrosc*, 2008, 69, 378-382.
112. S. Kumar, N. Matange, S. Umapathy and S. S. Visweswariah, *FEMS Microbiol Lett*, 2015, 362, 1-6.
113. K. L. Brown, O. Y. Palyvoda, J. S. Thakur, S. L. Nehlsen-Cannarella, O. R. Fagoaga, S. A. Gruber and G. W. Auner, *J Immunol Methods*, 2009, 340, 48-54.
114. G. Perna, M. Lastella, M. Lasalvia, E. Mezzenga and V. Capozzi, *J Mol Struct*, 2007, 834, 182-187.
115. Z. W. Huang, A. McWilliams, S. Lam, J. English, D. I. McLean, H. Lui and H. Zeng, *Int J Oncol*, 2003, 23, 649-655.
116. Z. W. Huang, A. McWilliams, H. Lui, D. I. McLean, S. Lam and H. S. Zeng, *Int J Cancer*, 2003, 107, 1047-1052.
117. M. G. N. Shim, Ph.D., The University of Toronto 2001.
118. H. Takeuchi and J. Sasamori, *Biopolymers*, 1995, 35, 359-367.
119. A. G. Shena, Y. Yea, J. W. Zhangb, X. H. Wanga, J. M. Hua, W. Xiea and S. J, *Vibrational Spectroscopy*, , 2005, 37, 225–231.
120. Y. S. Huang, T. Nakatsuka and H. O. Hamaguchi, *Appl Spectrosc*, 2007, 61, 1290-1294.
121. H. W. Wu, J. V. Volponi, A. E. Oliver, A. N. Parikh, B. A. Simmons and S. Singh, *P Natl Acad Sci USA*, 2011, 108, 3809-3814.
122. J. F. Christopher and I. M. Richard, *Anal Chem*, 1995, 67, 777-783.
123. B. S. Ran Li, M.Sc., The Ohio State University, 2013.
124. W. L. Lo, J. Y. Lai, S. E. Feinberg, K. Izumi, S. Y. Kao, C. S. Chang, A. Lin and H. K. Chiang, *J Raman Spectrosc*, 2011, 42, 174-178.

TABLE 1: ***Comparison of different methods of Ratio Analysis***

	Intensity Ratio	**Integrated Area Ratio**	**Curve fitted Area Ratio**
Description	Absolute intensity at a particular peak position is used	Whole area under the curve of a peak is used	The peak is curve fitted and area of de-convoluted peak is used
Difficulty level	Easy	Moderate	Hard
Performance when SNR is low (Weak peak)	Difficult to find the centre of a peak and sensitive to noise; not recommended	Provides authentic results	Provides authentic results if deconvolution done properly.
Performance when Peak is broad (Peaks convoluted by many bands)	Difficult to find the centre; try pure standard or standard addition	Can be used, suitable when peak bandwidth is changing	Provides authentic result if deconvolution done properly.
Strong/ Narrow peaks	Yields authentic results but not for peaks narrower than instrument resolution	Yields authentic results	Yields authentic results
Effect of Baseline correction and Smoothing 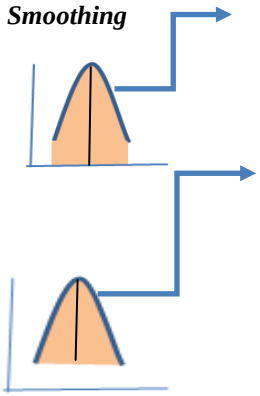	(a) Baseline correction critical when absolute intensity is measured from the axis. (b) Baseline correction does not affect when peak specific baseline is done. (c) Smoothing generally does not affect	(a) Baseline correction critical when absolute intensity is measured from the axis (b) Baseline correction does not affect when peak specific baseline is done. (c) Smoothing generally does not affect	(a) Baseline correction should be done carefully to get accurate fitting. (b) Deduction of no. of peaks is based on 2nd derivative analysis, which in turn depends on smoothing (c) Improper smoothing of 2nd derivative can lead to underestimation or over estimation of no. of peaks.
Effect of Normalization	Does not affect	Does not affect	Does not affect

Table 2: Library of IR ratios

Ratio (Xcm^{-1}/ Ycm^{-1})	Biomolecular Origin	Inference	System	
(850–900) / (900–1200) Δ	Total carbonate/ phosphate	Understanding mineralization process in tissues	Human bone tissue	14
966/996	DNA/RNA	Variation in nucleic acid content due to drug treatment	Mouse blood, liver and spleen tissues	27, 48
1013/1080	(Assignment unclear)/PO_2^- stretching	Measure of nuclear DNA damage after Fenton treatment	Human DNA	60
(1016-1020)/ (986-991) Δ	Polysaccharides/ DNA	Analysis of growth stages of cell culture	Fibroblast cells	26
1020 /1030	$HPO_4^{2-}$and/or CO_3^{2-}/ PO_4^{3-}	Measure of mineral crystallinity or maturity by the ratio of nonstoichiometric apatite/ stoichiometric apatite	Human bone tissue	14
1025/1082	Carbohydrates /phosphate	Classification of normal, cancerous and non-cancerous cervical tissue	Cervical cancer tissue	55
1030/1080	Glycogen / phosphate	Monitoring nucleic acid content following drug treatment. Detection of cervical cancer depicting altered metabolism in cancer cells. Potential biomarker to predict cell proliferation in normal or malignant tissue. Detection of oral cancer	Mouse liver tissue Cervical tissue Human oral cancer tissue	27, 48, 81, 82
(1030-1050)/ 1338 Δ	(CH_2OH + CO stretching)/ CH_2 wagging	Analysis of biochemical changes post-mortem	Rat liver and spleen tissue	83
(1063-1065)/ (1054-1056) Δ	Ribose/ saccharides	Differentiation of growth stages of cell culture. The ratio is higher for the exponential phase	Cultured fibroblast cells	26
1080/1338	PO_2^- (asym)/ CH_2 (wagging)	Analysis of changes in nucleic acid content post-mortem	Rat liver and spleen tissue	83
1080/1396	PO_2^-(sym)/ COO^- (sym)	Analysis of changes in nucleic acid content post-mortem	Rat and human kidney cortex tissue	61
1080/1540	PO_2^-	Proposed clinical parameter for the	Human leukaemia	14, 84

	(sym)/Amide II	evaluation of degree of malignancy Detection of Glucose-6-phosphate dehydrogenase (G6PD) deficiency	blood cells, Rabbit bone marrow fibroblast	
1080/1540 Δ	PO_2^- (sym)/Amide II	Detection of diabetes	Rat skeletal Soleus muscle tissue	54
1081/1532	PO_2^- / Amide II	Effect of drug treatment on tissue. The ratio is directly correlated to glycoprotein content	*Labeo rohita* finger lings	85
(1082-1056)/ 1028 Δ	Phosphate/ Glycogen	Discrimination of different premalignant stages	Mouse fibroblast cell lines, human cervical tissues	86
1084/1240	Glycogen/ Amide III	Detection of cervical cancer	Cervical tissue	55
1085/1046	Phosphate/ C-O-C of glycogen	Identification of gram positive and gram negative bacteria	Bacteria	62
1121/1015	RNA/DNA	Early detection and differentiation of premalignant stages of viral cancer	Mouse fibroblast cell lines, human cervical tissues	84, 86
1121/1020	RNA/DNA	Detection of cervical cancer or any type of malignancy. Discrimination of drug-resistant and non-resistant human melanoma cell lines	Cervical tissue Human cell	40, 86-88
1121/1020 (1121-903)/ (1020-903)	RNA/DNA	Grading of malignancy. Intensity value at 903cm^{-1} (internal reference) was subtracted from intensity value of 1121 and 1020 cm^{-1}	Lymphoid tissue	42
1121/1020 (1084-1020)/ (1084-1121)	RNA/DNA	Grading of malignancy. Intensity value at 1121 cm^{-1} and 1020 cm^{-1} were subtracted from the intensity value of 1084 cm^{-1} (internal reference)	Lymphoid tissue	42
(1130-1180)/ (1180-1260) Δ	Assignments not clear	Detection of cervical cancer	Cervical tissue	67
1151/1171	Cholesterol/ phospholipid	Differentiation of diabetic tissues from normal	Rat liver tissues	84
1153/1338	C-OH str/ CH_2 wagging	Analysis of chemical changes content post-mortem	Rat liver and spleen tissue	83
1155/1240 Δ	C-C str/ Amide III	Classification of normal and cancerous cervical cancer tissue based on ratio value	Human cervical tissue	84
1171/1151	Cholesteryl	Understanding of biochemical changes in	Mouse blood,	27, 48

	ester/ Glycogen & nucleic acids	infected liver, potential parameter for monitoring sepsis	liver and spleen tissues	
1171/1152	Protein/Carbo hydrate	Early detection and differentiation of premalignant stages of viral cancer	Mouse fibroblast cell lines, human cervical tissues	84, 86
1171/1152	Phospholipid / Cholesterol	Potential liver injury marker	APAP treated mouse liver tissue Mouse blood, liver and spleen tissues	48
(1231+1450)/ 1655	Collagen / Amide I	Classification of normal brain tissue, astrocytoma grade II and III, glioblastoma, haemorrhage and leptomeninges	Human brain tissue	41
1238/1338	PO_2^- (asym)/ CH_2 (wagging)	Analysis of biochemical changes post-mortem	Rat liver and spleen tissue	83
1238/1396	PO_2^- (asym)/ COO^- (Sym)	Analysis of biochemical changes content post-mortem	Rat and human kidney cortex tissue	61
1240/1084	Collagen/ nucleic acid	Identification of lymphoma grade cancer	Lymphoid tissue	42
1240/1312	Collagen / Amide III	Differentiation of normal brain tissue from different types of Glioblastoma (e.g. Fibriliary, Pleomorphic, Small, Giant, Lipidized)	Human brain tissues	57
1396/1456	COO^- (sym)/ CH_2 (asym deformation)	Analysis of biochemical changes content post-mortem. The ratio is correlated to fatty acid content	Rat liver and spleen tissue	83
1400/2852	Protein/Lipid	Differentiation of different growth stages of cell culture, greater for exponential phase	Cultured fibroblast cells	26
1452/1656	CH_2 bend/Amide I	Detection of diabetes	Rat skeletal Soleus muscle tissue	54
1452/1656 Δ	CH_2 bend/Amide I	Detection of diabetes	Rat skeletal Soleus muscle tissue	54
1453/1240	CH_3 bending/ CH_2 wagging	Index to distinguish between different stages of cancer	Human breast cancer tissue	89
1453/1396	CH_3 bending /	Differentiation of normal brain tissue from	Human brain	57

	CH_3 (sym)	different types of Glioblastoma (e.g. Fibriliary, Pleomorphic, Small, Giant, Lipidized)	tissue	
1454/1396	C-H_3 bending /COO^- (sym)	Analysis of fatty acid content post-mortem	Rat and human kidney cortex tissue	61
1516/1236	Amide II / Phosphate	Detection of liver metastasis with breast origin	Liver tissue	52
1532/1661	Amide II/ Amide I	Effect of drugs on tissue. A measure for protein content	*Labeo rohita* fingerlings	85
1532/3384	Protein/Lipid	Depiction of drug induced changes in tissues on the basis of the relative concentration of protein in membrane	*Labeo rohita* fingerlings	85
1540/1084	Amide II/ Phosphate Str	Grading of malignancy (ratio would be high for necrosis and sclerosis)	Human lymphoid tissue	42
1540/1343 Δ	Amide II/ collagen CH_2 vibration	Detection of diabetes	Rat skeletal Soleus muscle tissue	54
1541/1396	Amide II/ COO^- (sym str)	Analysis of biochemical changes content post-mortem	Rat and human kidney cortex tissue	61
1545/1080	Amide II/ Phosphodiester	Discrimination of epithelial cells from stromal cells	Cells	90
1553/1540	α helix/ Amide II	Differentiation of stages of cancer based on α helix content	Breast tumour tissue	91
1632 /1545	Amide I/ Amide II	The ratio changes with the amount of DNA in a cell, due to the contribution of DNA in amide I region. Determination of cell types, and stages of maturation. Identification of eye lens abnormalities	Cells Human eye lens	84
1647/1541	Amide I/ Amide II	Analysis of biochemical components post-mortem	Rat liver and spleen tissue	83
1651/1545	Amide I/ Amide II	Differentiation of stages of cancer based on α helix content	Breast tissue	91
1652/1396	Amide I/ COO^- (sym)	Analysis of biochemical components post-mortem	Rat and human kidney cortex tissue	61
1652/1541	Amide I/	Analysis of biochemical components post-	Rat and human	88

	Amide II	mortem	kidney cortex tissue	
1654/1545	Amide I/ amide II	Depiction of effect of CCl_4 treatment or radical aggregation in tissues	Rat liver and brain	92
1657/1204	Amide I/ collagen	Grading of different stages of cancer based on α helix content	Breast tumour tissue	91
1657/1278	Amide I /Collagen	Differentiation between cancer and normal tissue on the basis of collagen content based on α helix content	Breast tumour tissue	91
1657/1635	α helix/ β sheet	Grading of different stages of cancer	Breast tumour tissue	91
1658/1541	Amide I/ Amide II	Estimation of DNA content. Amide I band has contribution from DNA and proteins. The ratio change in the amount of DNA. Differentiation of brain tissue. The ratio is greater in grey matter than in white matter. Identification of different types of plaque. Differentiation of normal and cancerous cervical cancer	CNS tissue Cervical cancer tissue	88, 93
1660/1690 Δ	Amide I/ Carbonic acid	Assessing bone mineral content.	Lathyiritic rat bone	49
1680/1657	Turn/α helix	Grading of different stages of cancer based on information about collagen	Breast tumour tissue	91
1745/1468	Cholesterol esters/ CH_2 bending	Understanding of biochemical changes in infected liver, potential parameter for monitoring sepsis	Mouse blood, liver and spleen tissues	27, 48
2850/1655	Lipid /Amide I	Classification of normal brain tissue, astrocytoma grade 2 and 3, glioblastoma, haemorrhage and leptomeninges	Human brain tissue	41
2854/2873	CH_2 (sym) / CH_3 (asym)	Ratio corresponds with decrease in protein vs. lipid content. Detection of glucose-6-phosphate dehydrogenase (G6PD) deficiency	Rat liver and brain tissue	14, 51
2855/2929 Δ	CH_2 (sym)/CH_2 (asym)	Detection of diabetes	Rat skeletal Soleus muscle tissue	54
2858/3303	CH_2 (sym)/ Amide A	Analysis of biochemical changes post-mortem	Rat and human kidney cortex tissue	61

2871/3303	C-H str/ Amide A	Analysis of biochemical changes post-mortem	Rat and human kidney cortex tissue	61
2873/2852	Protein/Lipid	Understanding of biochemical changes in infected liver, potential parameter for monitoring sepsis	Mouse blood, liver and spleen tissues	27, 48
2925/2854	CH_2(asym) / CH_2 (sym)	Depiction of motional freedom in lipid acyl chains due to radical aggregation. A parameter for disorder in biological samples	Rat liver and brain tissue	92
2925/2855	CH_2 (asym) / CH_3 (sym)	Differentiation between drug treated and normal tissues	*Labeo rohita* fingerlings	85
2925/3303	CH_2 (asym)/ Amide A	Analysis of biochemical changes post-mortem	Rat and human kidney cortex tissue	61
2926+2959/ 3014	CH_2 (asym) + CH str./=CH str.	Monitoring chemical changes due to infection in tissues	Mouse liver tissues	51
2927/2855	CH_3(asym) / CH_2 (sym)	Estimation of protein content	*Labeo rohita* fingerlings	85
2929/2962 Area Ratio	CH_2 (asym)/CH_3 (asym)	Detection of diabetes. The ratio depicts chain length.	Rat skeletal Soleus muscle tissue	54
(2929+2855)/ 3012 Δ	CH_2 (asym) + CH_2 sym/olefinic	Detection of diabetes based on saturated/unsaturated content	Rat skeletal Soleus muscle tissue	54
2929+2855/ 1452 Δ	CH_2 (asym) + CH_2 (sym)/CH_2 bending	Detection of diabetes	Rat skeletal Soleus muscle tissue	54
2958/ (2852+2923)	Lipids/Protein	Early detection and differentiation of premalignant stages of viral cancer	Mouse fibroblast cell lines, human Cervical tissues	84
2958/2853	CH str/ CH_2 str	Discrimination between drug-resistant and non-resistant human melanoma cell lines	Human cell	86
2958/2921	CH_3 (asym) / CH_2 (asym).	Detection of tumour progression based on mean saturation level of lipids	Human tissue	40
2958/2925	CH_3(asym) / CH_2 (asym)	Detection of in vivo radical aggregation	Rat liver and brain tissue	92
2958/3303	CH_3 (asym)/	Understanding of chemical changes post-	Rat and human	61

	Amide A	mortem	kidney cortex tissue	
2959/3014	CH_3 (asym) / olefinic =CH stretch	Detection of in vivo radical aggregation based on motional freedom of microsomal membrane	Rat liver and brain tissue	51
2965/2930	CH_3 (from proteins) / CH_2 (from phospholipids)	Identification of eye lens abnormalities: normal vs. cataractous, without glaucoma vs. glaucomatous lenses	Cataractous lenses with glaucoma	14
3012/2958	CH(asym) / CH_3 (asym)	Detection of tumour progression based on mean unsaturation level in lipids	Human tissue	40
3012/3303	CH(asym) / Amide A	Understanding of chemical changes post-mortem	Rat and human kidney cortex tissue	61
3100-2800 Δ	CH(asym)/ CH_3(sym)	Evaluation of amount of glucose based on amount of lactic acid absorbed	U87 glioma and A54918 adenocarcinoma cells	94
3100-2800 Δ	CH_2 (asym)/ CH_3 (asym)	Measurement of glucose level	U87 glioma and A54918 adenocarcinoma cells	94
3300/3075	Amide A/ Amide B	Grading of breast cancer	Breast tumour tissue	91
3303/2925	Amide A/CH_2 (asym)	Analysis of biochemical changes post-mortem	Rat liver and spleen tissue	83

*Abbreviations used: sym - Symmetric Stretching mode; asym - Asymmetric Stretching mode; str - Stretching mode;*Δ- Area ratio

Table 3: Library of Raman Ratios

Ratio Xcm^{-1}/ Ycm^{-1}	Bio-molecular Origin	Inference	System	Ref
643 /(823+854)	C-C twist of Tyr/ sum of ring breathing modes of Tyr	Used to check the DNA contamination in protein	Bacterial protein	95
656/725	Trp/ Adenine & coenzyme A	Differentiation of cancerous and non-cancerous tissue. Ratio increased for cancerous tissue. By SERS method	Thyroid tissue	78
668/1447	C-S str Cysteine/CH_2 bending	Assessment of Reactive Oxygen Species (ROS) in cells induced by Carbon Nanoparticles.	MCF-7 cell line	64, 96
721/754	+C-H bend/Trp	Classification of normal, dysplastic and cancerous larynx	Human larynx	97
724/738	Assignment not mentioned in the reference	Screening method for getting genomic information in DNA duplexes by SERS	DNA	98
725/1268	DNA/ Amide III	Marker band for monitoring DNA damage.	Human mesenchymal stem cells	99
732/788	Assignment not mentioned in the reference	Quantification of relative methylated base populations by SERS	DNA	98
743/730	Assignment not mentioned in the reference	Quantification of relative methylated base populations by SERS	DNA	98
754/780	Trp/ Unassigned by author	Classification of normal, dysplastic and cancerous larynx	Human larynx	97
757 or 853/784	Trp or Tyr/ DNA	Differentiation between stem cell and differentiated cells by Raman, stimulated Raman	Stem cells	100
760/1452	Trp/ CH_2 deformation	Understanding muscle contraction and relation mechanism	Muscle fibres from giant barnacle	101
781/787	DNA/RNA	Classification of benign prostatic hypertrophy (BPH) and prostate adenocarcinoma (CaP)	Prostate tissue	102
783/1004	PO_2 of DNA /Phenylalanine	Classification of species by laser tweezer Raman spectroscopy	Bacteria	103
785/1002	PO_2 of DNA	Quantification of DNA due to antibiotic	Bacteria	104

	/Phenylalanine	treatment		
785/1092	DNA/ DNA	Indicative of the efficiency of DNA packaging process. Discriminate sperm of normal, pear, small and double head,	Human sperm	102
786/1003	DNA/Phe	Decrease in this ratio observed when cells move to apoptosis phase	Human embryonic lung fibroblast cells	105
828/754	Tyr/Trp	Classification of normal, dysplastic and cancerous larynx	Human larynx	97
854/823	Tyrosine /Tyrosine Ring breathing modes	Diagnostic of the H-bonding environment of tyrosine	Bacterial protein	95
855/830	Tyr Fermi resonance doublet	Sensitive to H-bonding of phenolic OH environment by SERS	Bovine Serum Album (BSA)	106
875/ 1450	Hydroxy proline/ CH_2 bend	Differentiation between normal and dysplastic gastric tissue	Gastric tissue	107
880/937 Δ	Proteins(Pro, Val, Trp)/ α helix, Pro, keratin proteins	Differentiation of resistant and sensitive testicular cancer cell lines	Testicular cancer cell line	108
(900–1000) /(1590–1720) Δ	phosphate/ amide I	Mineral-to-matrix ratio	Teeth	109
928-940 /1450	C-C str/ CH_2	Marker band for differentiating cancerous and non-cancerous tissue, when 4 different types of tissue are examined. Ratio was high for cancerous	Breast, colon, pancreas and thyroid tissue	110
936/956	Pro, Val & α helix/ Assignment unclear	Classification of normal, dysplastic and cancerous larynx	Human larynx	97
937/ 1209	C-C str , Pro, Val/ Phe & Tyr	Differentiation cancerous and non-cancerous cells by SERS	human hepatoma carcinoma and human hepatic cell lines	76
1005/1013	Phe/Trp	Understanding Changes due to	Lysozyme	106

		temperature by SERS and 2D correlation		
1016/785	Trp/Trp	Monitoring culture condition (UV RRS)	*E.coli* and *B.subtilis*	63
1033/1005	Phe/Phe	Changes due to temperature by SERS and 2D correlation	Lysozyme	106
1050/1095	Both peaks are due to DNA phosphate backbone	Ratio is indicative of nuclear damage due to oxidative stress.	Sperm nuclear DNA	60
1070/960	Carbonates/Phosphates	Carbonate-to-phosphate ratio	Teeth	109
1147-1271/ 1450	N-H bend/ CH_2	Marker band for differentiating cancerous and non-cancerous tissue	Breast, colon, pancreas and thyroid tissue	110
1155/1172	C-N proteins, carotenoids/	Classification of Normal, Dysplastic and Cancerous Larynx	Human larynx	97
1156/I_{max}	Carotenoids/intense band in the spectrum	Detection of cancer. I_{max} used for normal is 1452 or 1587 cm^{-1}; for malignant is 1452, 1522 or 1660.	Gastric mucosa tissue	111
1156/1658	Carotenoids/Amide I	Effect of carbon source on bacterial biochemical composition	*M.smegmatis*	112
1182/1070	Assignment not defined in the reference	Diagnosis of dysplasia vs. inflammation and dysplasia vs. metaplasia	Human cervix tissue	21
1182/1195	Assignment unclear	Differentiation of activated, inactivated and resting T lymphocytes	Human T lymphocyte cells	113
1182/1454	Assignment unclear/ collagen+ phospholipid	Diagnosis of dysplasia vs. normal	Human cervix tissue	21
1195/1070	Assignment not defined in the reference	Diagnosis of dysplasia vs. inflammation and dysplasia vs. normal	Human cervix tissue	21
1265/1336	Amide III/ collagen & polynucleotide	Classification of normal, dysplastic and cancerous larynx	Human larynx	97
1276/1308	Amide III/ CH_2 twists of nucleic	Differentiation of cancerous and non-cancerous cells by SERS	human hepatoma carcinoma and	76

	acids		human hepatic cell lines	
1287/1268	DNA/Amide III	Marker band for monitoring DNA damage.	Keratinocyte cells	114
1290-1360/ 1220-1290 Δ	C-H bending/ Amide III	Differentiation of normal skin and basal cell carcinoma	Human skin	75
1302/ 1265	CH_2 bend/ Amide III	Detection of cancer. Ratio decreased in tumour tissue. Effect of formalin fixation also	Bronchial normal and cancer tissue	115, 116
1302/1268	Phospholipids/ Amide III	Marker for cell membrane damage. Inverse relation with cytotoxicity	Human mesenchymal stem cells	114
1303/1264	CH_2/methyl def	Measurement of unsaturated lipids. Corticol lipids were 14% more saturated than nuclear.	Human eye lens	117
1315/1336	Collagen/ collagen & polynucleotide	Classification of normal, dysplastic and cancerous larynx	Human larynx	97
1330/ 1454	DNA/ collagen & phospholipid	Discrimination high-grade squamous dysplasia from all others	Human cervix tissue	21
1330/1480	Adenine/ adenine & guanine	Indication of nucleotide base stacking. Ratio Increased for malignant cells. (UV RRS)	Breast and cervical cancer cells	56
1336/1481	Adenine/adenine & guanine	Understanding interaction of protein and nucleotide (UV RRS)	Nucleotide and histone proteins	118
1338/1268	DNA/Amide III	Marker band for DNA damage.	Keratinocyte Cells	114
1342/1375	Adenine & guanine / thymine	Differentiation of cancerous and non-cancerous cells by SERS	human hepatoma carcinoma and human hepatic cell lines	76
1360/1340	Tryptophan Fermi doublet	Sensitive to the environment and phenolic H bond (UV RRS)	Haemoglobin fibres	80
1360/1380	Tryptophan Fermi doublet	Hydropathicity of ring environment	Bacterial protein	95
1400/1070	Assignment not defined in the reference	Diagnosis of dysplasia vs. inflammation	Human cervix tissue	21
1400/1454	assignment unclear/	Diagnosis of dysplasia vs. inflammation	Human cervix tissue	21

	collagen+ phospholipid			
1402/1435	CH_3 proteins/ CH_3 asym deformation	Differentiation of cancerous and non-cancerous cells by SERS	Human hepatoma carcinoma and Human hepatic cell lines	76
1404/1436	Assignment unclear/ CH_2 def	Understanding interaction of repressor protein with antibiotic	Bacterial protein	95
1405/1452	Assignment unclear/ CH_2 deformation	Understanding muscle contraction and relation mechanism	Muscle fibres from giant barnacle	101
1441/1652	Phospholipids/proteins & phospholipids	Detection of cancer	Breast tissue	74
1442/1667	CH_2 bend/ C=C str	Differentiation of normal adipose tissue and liposarcoma	adipose tissue	97
1445/1655	CH_2/Amide I	Differentiation of non-malignant and malignant tissue	Bronchial tissue	115, 116
1445/1655	Phospholipids/ Amide I	Detection of cancer. Ratio decreased in tumour tissue. Effect of formalin fixation also analysed for bronchial tissue	Bronchial and lung tissue	108
1449/1418	Lipids/Trp, C-H bending modes	Differentiation of seminal plasma	Human seminal Plasma	79
1452/1660	CH_2 lipids/ Amide I	Ratio does not distinguish cancerous and non-cancerous tissue well	Cervical tissue	74
1454 /1656	Collagen+ phospholipid/ (collagen + Amide I)	Diagnosis of dysplasia vs. inflammation and dysplasia vs. normal	Human cervix tissue	21
1454/1330	Collagen+ phospholipid /DNA	Diagnosis of dysplasia vs. normal	Human cervix tissue	21
1459/1100	Protein/ lipid	Classification of benign prostatic hypertrophy (BPH) and prostate adenocarcinoma (CaP)	Prostate tissue	102
1480/1540	Nucleic Acid/ DNA & protein	Differentiation of malignant cells versus normal cells. (UV RRS)	Breast and cervical cancer cells	56
1480/1614	Adenine &	Differentiation of malignant cells	Breast and cervical	56

	guanine/Trp &Tyr	versus normal cells (UV RRS)	cancer cells	
1485/ 1616	Nucleic acids/ Proteins	Sensitive to growth phase of the cells. Ratio increased for log phase cells. (UV RRS)	Breast and cervical cancer cells	56
1524/1658	Carotenoids/Amide I	Effect of carbon source on bacterial biochemical composition	*M. smegmatis*	112
1525/1156	C=C of carotenoid/ C-C of carotenoid	Ratio increases in malignant gastric mucosa	Gastric carcinoma cell line	119
1530/1485	Cytosine/ adenine& guanine	Direct correlation to the A-T /G-C ratio in cells (UV RRS)	Breast and cervical cancer cells	56
1555/1210	Trp/Tyr	Sensitive to gram type of bacteria (UV RRS)	*E.coli* and *B.subtilis*	63
1556/1616	Trp/Trp & Tyr	Independent of media and growth condition (UV RRS)	Breast and cervical cancer cells	56
1575/1616	Nucleic acids/ proteins	Sensitive to growth phase of the cells, Ratio increased for log phase cells. (UV RRS)	Breast and cervical cancer cells	56
1587/ 1605	Trp/ Phe & Tyr	Differentiating meningeal cancer tissue from the benign and normal meningeal tissue. (RRS)	Brain cancer tissue	58
1587/ I_{max}	Lipids or retinol /intense band in the spectrum	Detection of cancer. I_{max} used for normal is 1452 or 1587 cm^{-1}; for malignant are 1452, 1522 or 1660.	Gastric mucosa tissue	111
1587/1156	Lipids or retinol/ carotenoids	Detection of cancer. Ratio decreased in malignant tissue	Gastric mucosa tissue	111
1602/1655	Tyr, Phe, Trp/Amide 1	Understanding metabolic changes in mitochondria. 1602 cm^{-1} Noted as "Raman Signature of life"	*S. pombe* cells	120
1603/1615	Phe/Trp	Classification of Normal, Dysplastic and Cancerous Larynx	Human larynx	97
1618/1555	Trp & Tyr/Trp	Differentiation of gram positive and gram negative bacteria by UV RRS. Ratio increased for gram positive bacteria.	*E.coli* and *B.subtilis*	63
1650/ 1440	C=C stretch/	In vivo quantification of Unsaturated	Algae	121

	CH_2 bend	lipids and melting temperature using Laser Tweezer Raman.		
1654/1439 Δ	Amide I/ CH_2	Direct correlation with degree of fatty acid unsaturation. Grading and typing of cancer	Breast cancer tissue	122
1654/1746	C=C str/C=O str	Measure for fatty acid content in tissues. Level of unsaturated fatty acid is higher in colon compared to prostrate and pancreas	Colon, pancreas and prostrate tissue	123
1655/1450	Amide I/ CH_2	Marker band for Differentiating cancerous and non-cancerous tissue	Breast, colon, pancreas and thyroid tissue	110
1656/1454	Collagen + Amide I/ phospholipid+ collagen	Diagnosis of dysplasia vs. metaplasia.	Human cervix tissue	21
1660/1004 Δ	Amide I/ phenylalanine	Understanding the maturation process of Ex-Vivo Produced Oral Mucosa Equivalent (EVPOME)	human oral mucosal keratinocytes	124
1660/1450	Amide I/ CH_2 bend	Detection of gastric carcinoma cells in the human malignant gastric mucosa	Gastric carcinoma cell line	119
1660/1690	Pyridinoline crosslinks/dehydro dihydroxylysino norleucine crosslinks	Measure of collagen crosslinking changes. Deduced from the bands contained within the Amide I	Teeth	109
1760/1070	Assignment not defined in the reference	Diagnosis of normal vs. inflammation	Human cervix tissue	21
2886/2850	CH_2/CH_2	Measure of disorder and indication of fluidity of lipids	Human eye lens	117
2935/2886	Fermi resonance of fat and proteins / poly methylene chain	Differentiating meningeal cancer tissue from the benign and normal meningeal tissue (RRS)	Brain cancer tissue	58
(3000-2800)/ 952 Δ	C-H peaks/ sym phosphate	Measurement of collagen upon deproteination	Bone	108

Abbreviations used: Tyr –Tyrosine, Trp –Tryptophan, Phe- Phenylalanine, Sym - Symmetric Stretching mode, Asym -Asymmetric Stretching mode, Str- Stretching mode. SERS- Surface Enhanced Raman Spectroscopy. RRS- Resonance Raman Spectroscopy, UV- Ultraviolet, Δ- Area Ratio.

Figure legends:

Figure 1: Flow chart of Vibrational Spectral Analysis Steps

Figure 2: Peak intensity ratio is not affected by fluctuations in laser power: (i) Raman spectra of a U87 cell line recorded at 785 nm with different laser powers: ~ 10 mW, 19 mW, 54 mW and 107 mW. (ii) Variation in absolute intensity of the 1440 cm^{-1} band with increasing laser power. (iii) Peak intensity ratio of the 1003/1440 bands with increasing laser power. Each spectrum depicted here is the average of 50 spectra taken from various regions of the cells. Spectra are shown without any processing. (1003 cm^{-1}: Symmetric ring breathing of phenylalanine; 1440 cm^{-1}: CH_2 deformation mode)

Figure 3: Influence of the water background on the peak intensity ratio: (i) Raman spectra of a U87 cell line recorded at 785 nm. The red spectrum (top) is obtained after subtraction of the PBS background; the blue curve (middle) shows the raw spectrum and the black curve (bottom) shows the PBS spectrum (ii) Peak intensity ratio of the 1440/1660 bands before and after background subtraction. Each spectrum shown here is the average of 50 spectra taken from different regions of the cells. Statistical analysis was performed using unpaired Student's t-test; $p< 0.05$ was considered to be statistically significant;* represents $p< 0.05$. (1440 cm^{-1}: CH_2 deformation mode; 1660 cm^{-1}: Amide I band)

Figure 4: Dependence of peak intensity ratios and peak area ratios on baseline variations: Raman spectra of plasmid DNA recorded at 633 nm and 785 nm. (i) With baseline correction. (ii) Without baseline correction. (iii) Peak intensity ratio of the 1480/1580 bands (nearby peaks) with/without baseline correction at 633 nm and 785 nm. (iv) Peak intensity ratio of the 785/1580 bands (distant peaks) with/without baseline correction at 633 nm and 785 nm. (v) Peak area ratio of the 1480/1580 bands (nearby peaks) with/without baseline correction at 633 nm and 785 nm. (vi) Peak area ratio of the 785/1580 bands (distant peaks) with/without baseline correction at 633 nm and 785 nm. Each spectrum shown here represents the average of 10 spectra taken from different regions of the DNA droplet. In (i), spectra were baseline corrected using a 10th order polynomial fitting. In (ii), no pre-processing was done. (1480 cm^{-1}: Amide II; 1580: Pyrimidine ring (nucleic acids); 785 cm^{-1}: Uracil (U), Thymidine (T), Cytosine (C) ring breathing modes in DNA)

Figure 5: Influence of sample thickness on peak intensities and peak ratios: (i) Bright field image of Bovine Serum Albumin (BSA) drop cast on a calcium fluoride coverslip. Yellow arrows indicate thick and thin regions of the BSA drop. (ii) Raman line map (step size: 1 µm) recorded at 633 nm showing intensity variations of the 1003 cm^{-1} band across the sample. (iii) Variations in the 1003/1660 band ratio across

the sample. (iv) Graphical representation of the variation of the absolute intensity at 1003 cm^{-1} and the ratio of the 1003/1660 bands during the line scan, illustrating how ratioing can compensate for the influence of sample thickness. (v) Comparison of Standard Deviation calculated for the ratio from 0-30 µm of the mapped area and from 30-100 µm. Statistical analysis was performed using unpaired Student's t-test.; $p< 0.05$ was considered to be statistically significant;** represents $p< 0.01$. (1003 cm^{-1}: Symmetric ring breathing of phenylalanine; 1660 cm^{-1}: Amide I band)

Figure 6: Different methods of ratio calculation: (i) FTIR spectrum of BSA. (ii) Raman spectrum of BSA. (iii) Illustration of Absolute intensity based (a), Peak area based (b) and Curve fitted area based (c) ratioing methods using the Amide I band in the FTIR spectrum. (iv) Deconvolution of the 1220-1360 cm^{-1} region of the Raman spectrum. (v) Ratio of the 1657/1545 bands calculated from the FTIR spectra of BSA using the above mentioned methods. (v) Ratio of the 1448/1654 bands calculated from the Raman spectra of BSA using the above mentioned approaches. The FTIR and Raman spectra shown above are the averages of 10 spectra taken from different regions of the BSA drop edge. (1657 cm^{-1}: Amide I (α helix); 1545 cm^{-1}: Amide II)

Figure 7: Deconvolution of FTIR spectrum of BSA: (i) The black curve (full line) indicate the original spectrum. Cyan colour indicates the cumulative fit using three bands, shown in pink, purple and blue colours. (ii) Absolute intensity ratio of the 1081/1125 bands, calculated using the curve fitting method as well as based on the raw intensity data. (1081 cm^{-1}: PO_2^- symmetric stretch; 1109 cm^{-1}: C-N stretch; 1125 cm^{-1}: C-O stretch)

Figure 8: Infrared imaging of mouse kidney tissue section: (i) Bright field image of a 4 µm thick mouse kidney tissue section. (ii) IR images mapped using maximum intensities of the 1537 and 1650 cm^{-1} bands and their ratio 1537/1650 , IR images mapped using area intensity with centre at 1537 and 1650 and area ratio of 1537/1650 (iii) Principal Component Analysis image of kidney tissue section. The scales of IR intensity, ratio and PCA maps were kept between 0 and 1(A.U.) whereas the area was scaled from 0 to 30 arbitrary units (A.U.) (1537 cm^{-1}: Stretching C=N/ C=C; 1650 cm^{-1}: Amide I band)

Figure 9: **Raman imaging of mouse kidney tissue section:** (i) Bright field image of a 10 µm thick section. (ii) Raman images mapped using area based intensity at 1660, at 1440 cm^{-1} and the ratio of the 1440/1660 bands. The scales were adjusted between 0 and 300000 A.U. for area maps and from 0 to 1 A.U. for ratio maps. (1440 cm^{-1}: CH_2 bending; 1660 cm^{-1}: Amide I band)

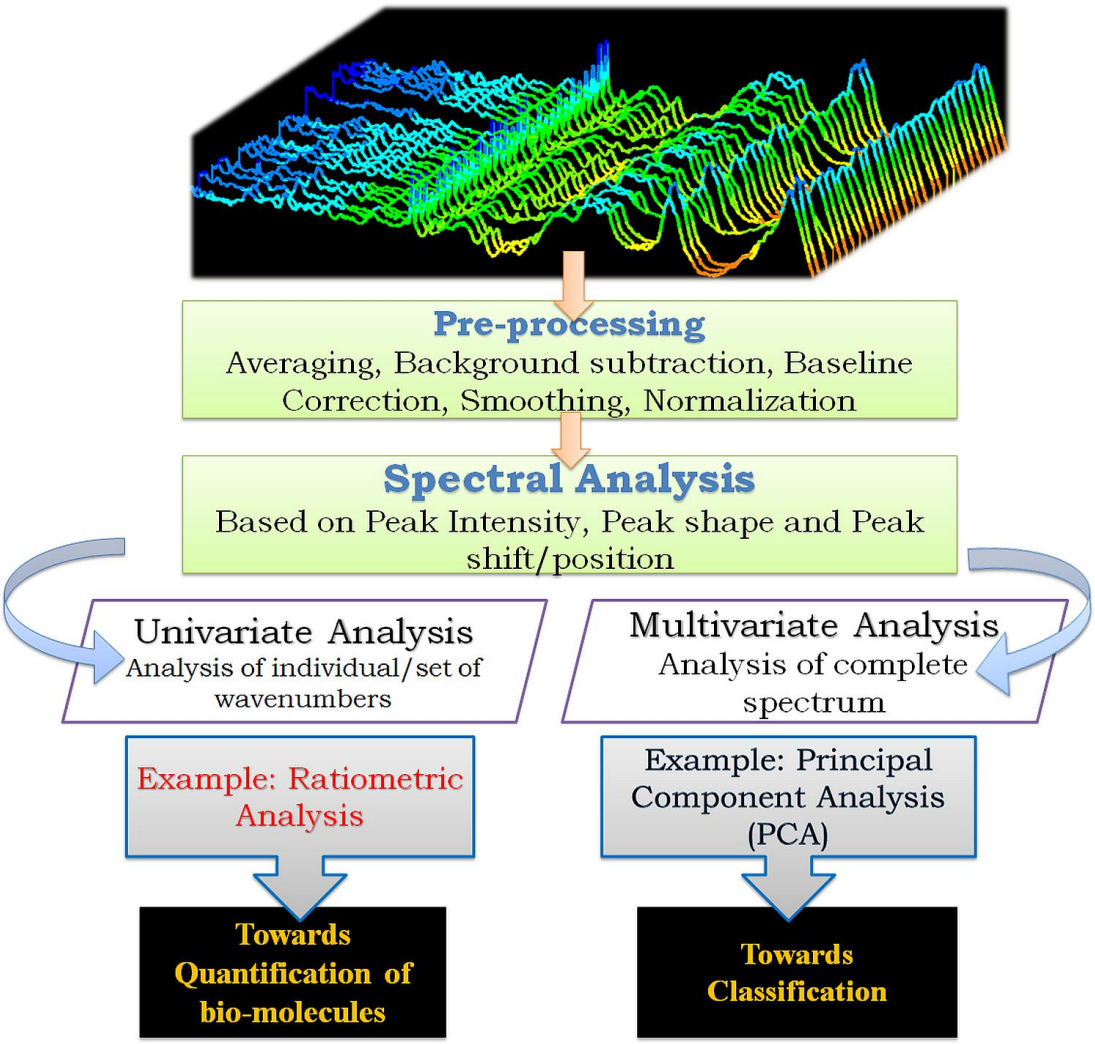
Pre-processing
Averaging, Background subtraction, Baseline Correction, Smoothing, Normalization
Spectral Analysis
Based on Peak Intensity, Peak shape and Peak shift/position
Univariate Analysis
Analysis of individual/set of wavenumbers
Multivariate Analysis
Analysis of complete spectrum
Example: Ratiometric Analysis
Example: Principal Component Analysis (PCA)
Towards Quantification of bio-molecules
Towards Classification

Figure 1

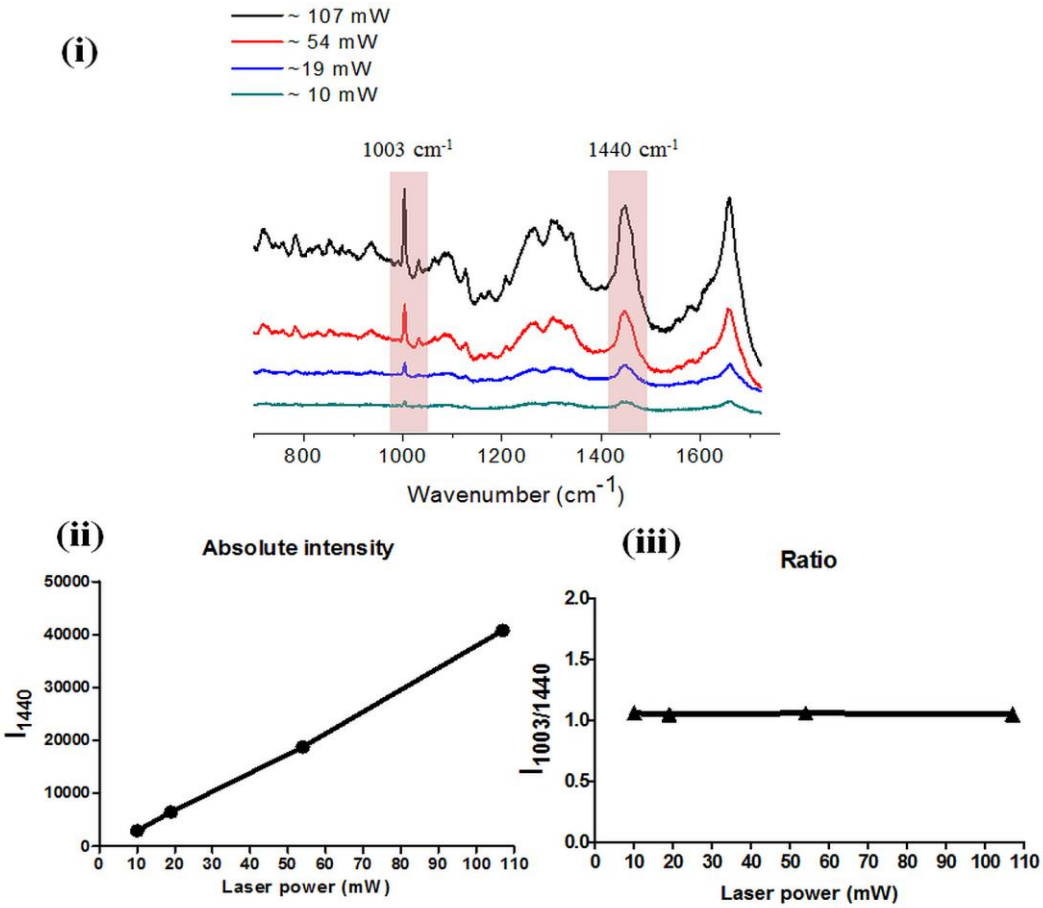

Figure 2

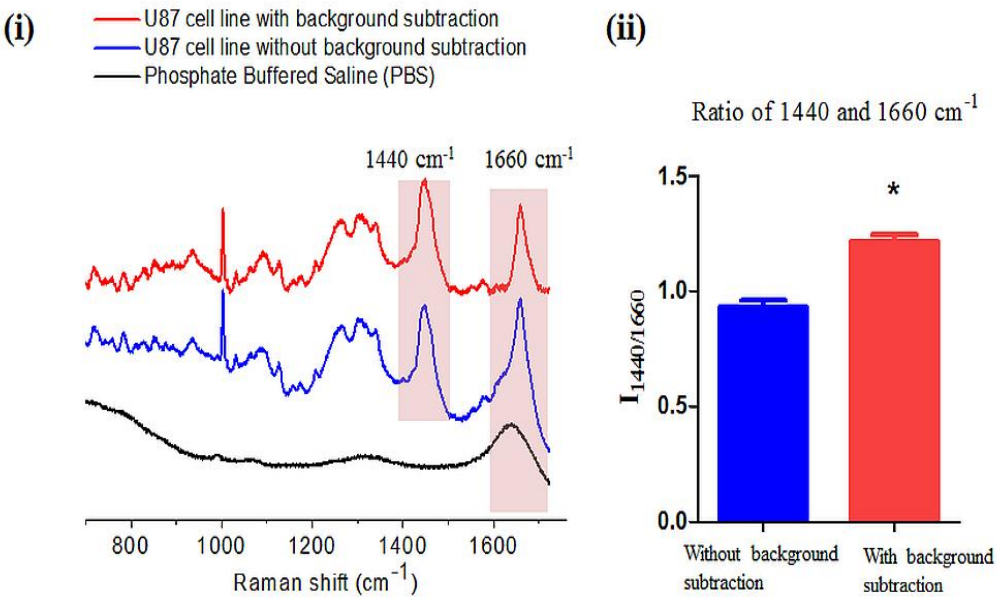

Figure 3

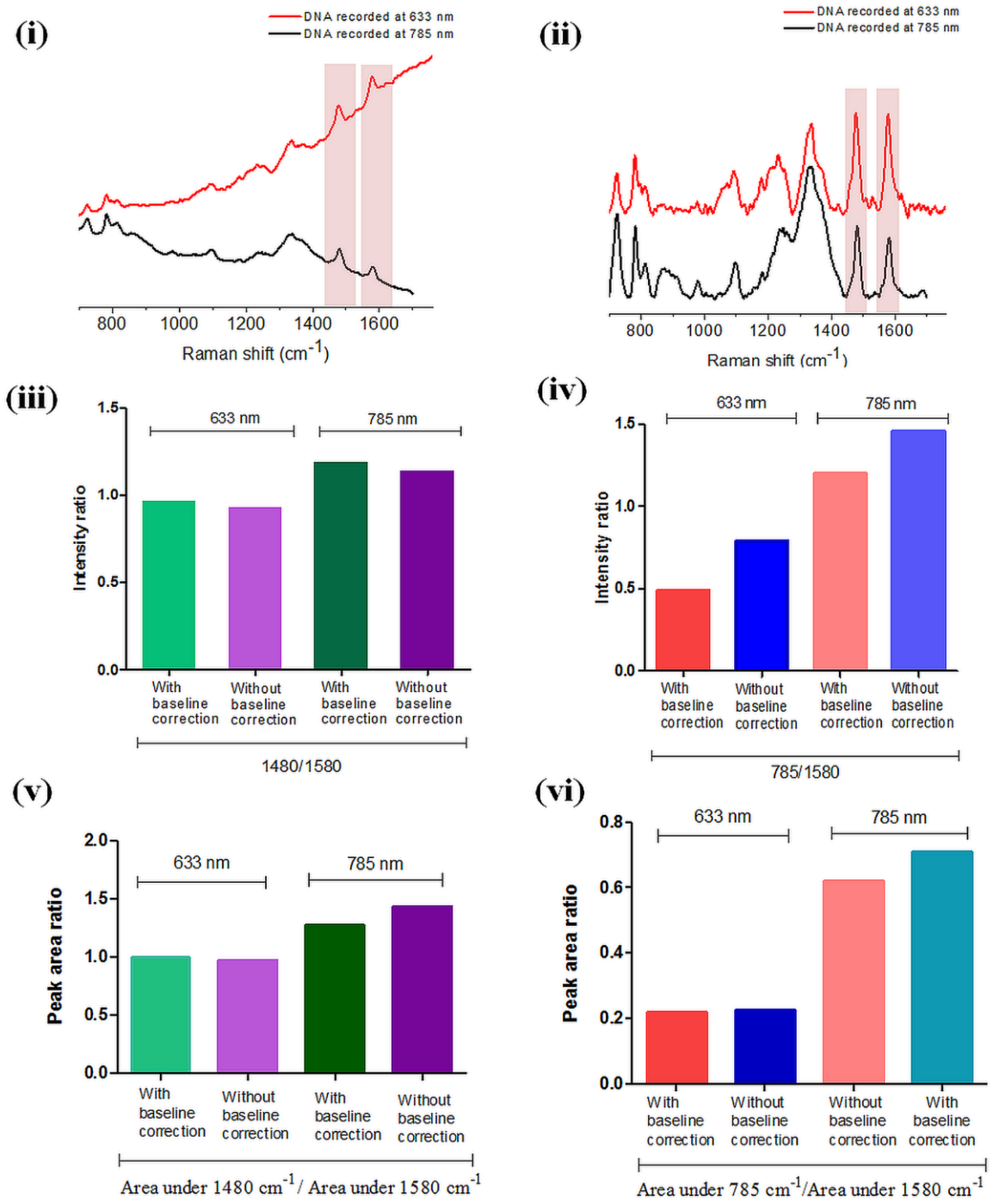
(i)
DNA recorded at 633 nm
DNA recorded at 785 nm
800
1000
1200
1400
1600
Raman shift (cm-1)
(ii)
DNA recorded at 633 nm
DNA recorded at 785 nm
800
1000
1200
1400
1600
Raman shift (cm-1)
(iii)
633 nm
785 nm
Intensity ratio
1.5
1.0
0.5
0.0
With baseline correction
Without baseline correction
With baseline correction
Without baseline correction
1480/1580
(iv)
633 nm
785 nm
Intensity ratio
1.5
1.0
0.5
0.0
With baseline correction
Without baseline correction
With baseline correction
Without baseline correction
785/1580
(v)
633 nm
785 nm
Peak area ratio
2.0
1.5
1.0
0.5
0.0
With baseline correction
Without baseline correction
With baseline correction
Without baseline correction
Area under 1480 cm-1 / Area under 1580 cm-1
(vi)
633 nm
785 nm
Peak area ratio
0.8
0.6
0.4
0.2
0.0
With baseline correction
Without baseline correction
Without baseline correction
With baseline correction
Area under 785 cm-1/Area under 1580 cm-1

Figure 4

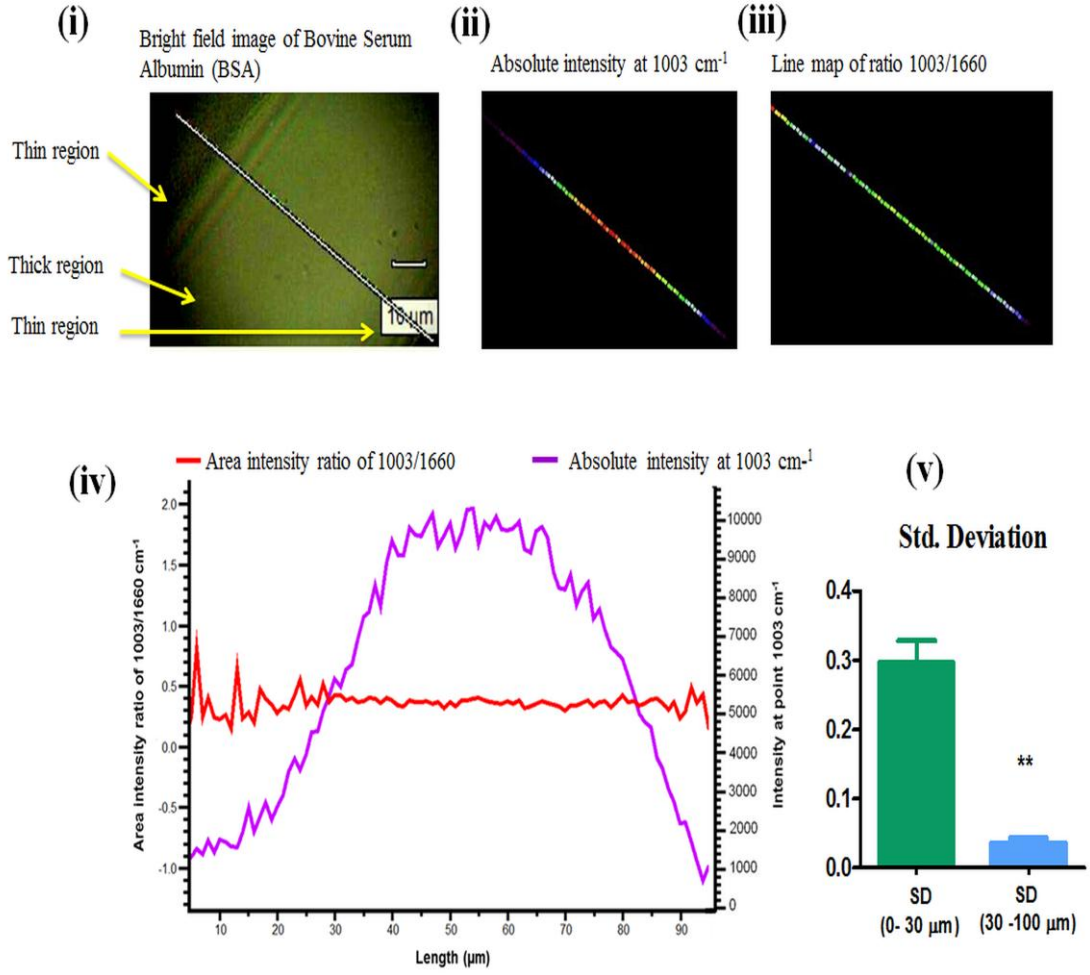
(i)
Bright field image of Bovine Serum Albumin (BSA)
Thin region
Thick region
Thin region
16 µm
(ii)
Absolute intensity at 1003 cm-1
(iii)
Line map of ratio 1003/1660
(iv)
Area intensity ratio of 1003/1660
Absolute intensity at 1003 cm-1
Area intensity ratio of 1003/1660 cm-1
Intensity at point 1003 cm-1
Length (µm)
(v)
Std. Deviation
**
SD (0- 30 µm)
SD (30 -100 µm)

Figure 5

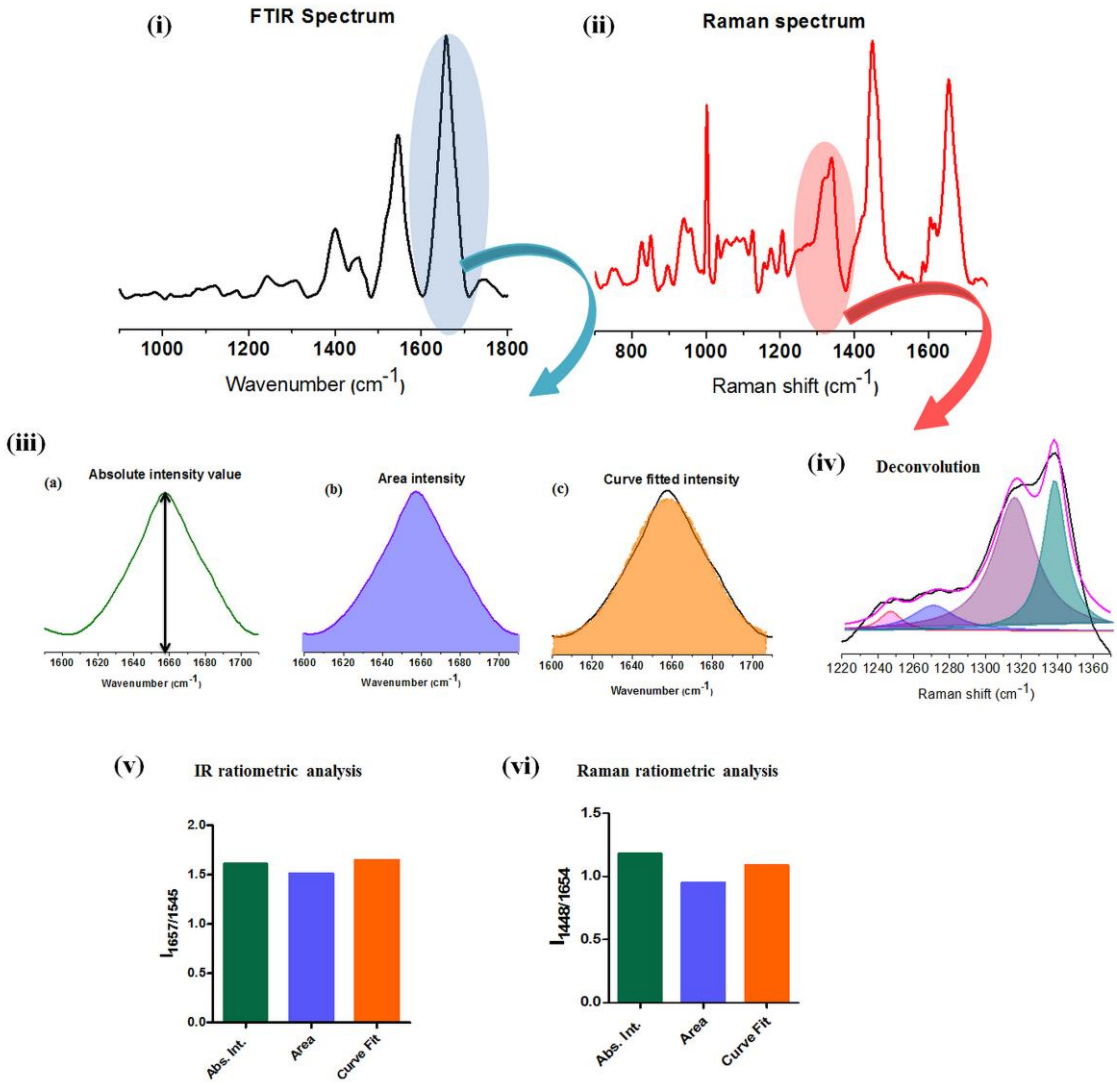
(i)
FTIR Spectrum
1000 1200 1400 1600 1800
Wavenumber (cm-1)
(ii)
Raman spectrum
800 1000 1200 1400 1600
Raman shift (cm-1)
(iii)
(a)
Absolute intensity value
(b)
Area intensity
(c)
Curve fitted intensity
1600 1620 1640 1660 1680 1700
Wavenumber (cm-1)
(iv)
Deconvolution
1220 1240 1260 1280 1300 1320 1340 1360
Raman shift (cm-1)
(v)
IR ratiometric analysis
I1657/1545
Abs. Int.
Area
Curve Fit
(vi)
Raman ratiometric analysis
I1448/1654
Abs. Int.
Area
Curve Fit

Figure 6

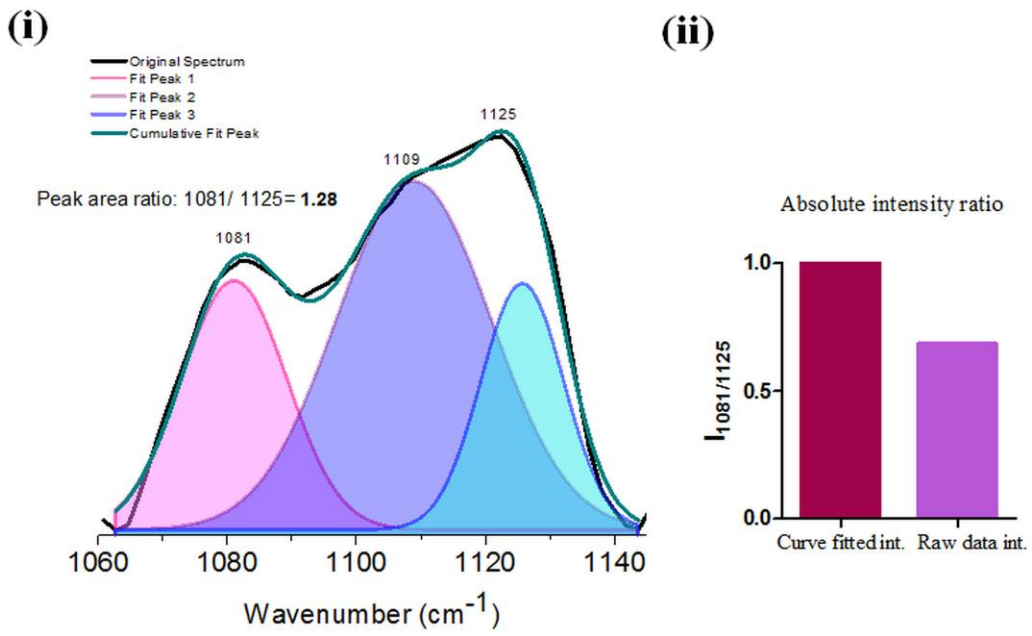
(i)
Original Spectrum
Fit Peak 1
Fit Peak 2
Fit Peak 3
Cumulative Fit Peak
1125
1109
1081
Peak area ratio: 1081/ 1125= 1.28
1060
1080
1100
1120
1140
Wavenumber (cm-1)
(ii)
Absolute intensity ratio
I1081/1125
1.0
0.5
0.0
Curve fitted int.
Raw data int.

Figure 7

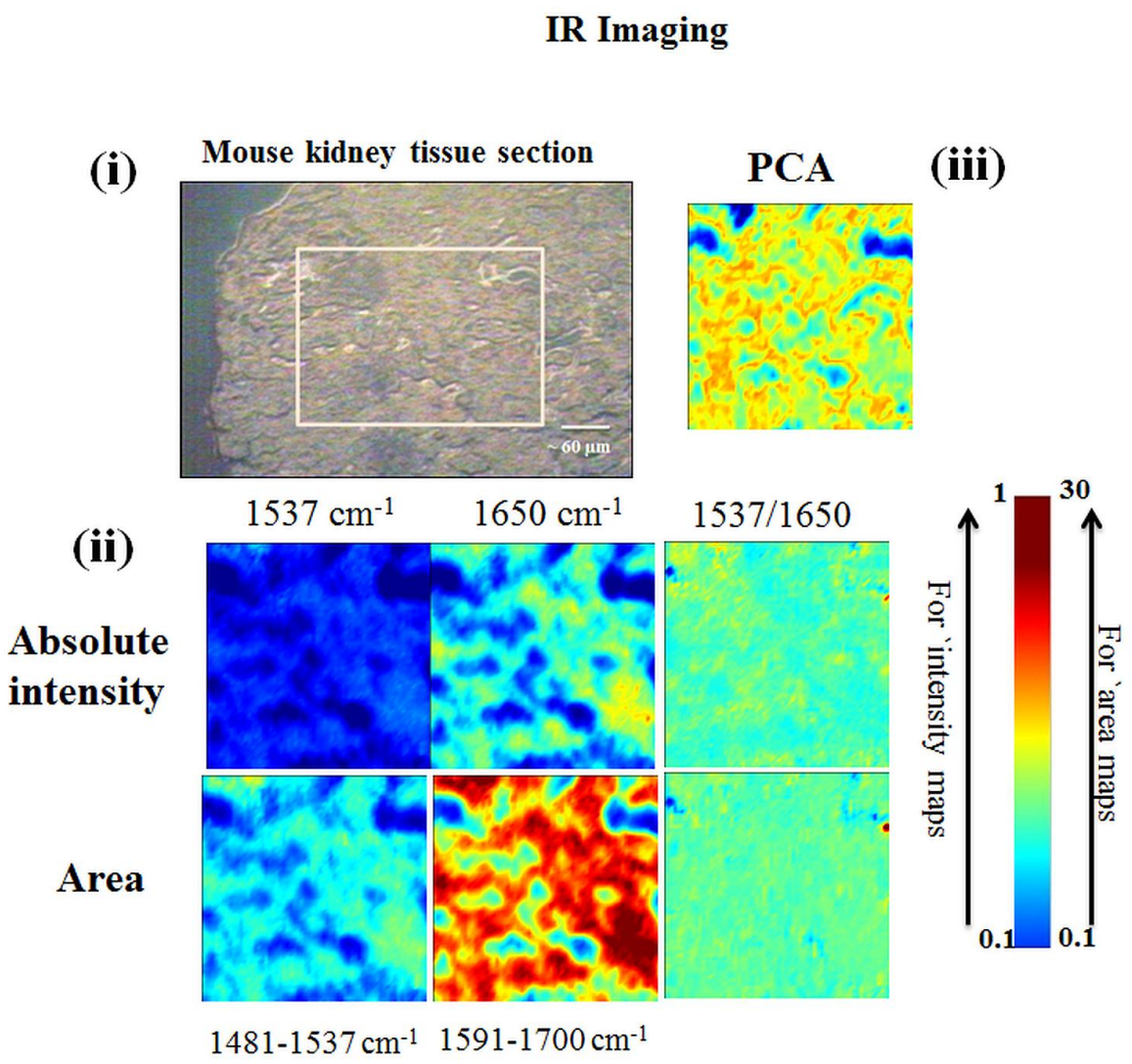
IR Imaging
(i)
Mouse kidney tissue section
~60 µm
PCA
(iii)
(ii)
1537 cm-1
1650 cm-1
1537/1650
Absolute intensity
Area
1481-1537 cm-1
1591-1700 cm-1
1
30
0.1
0.1
For 'intensity maps
For 'area maps

Figure 8

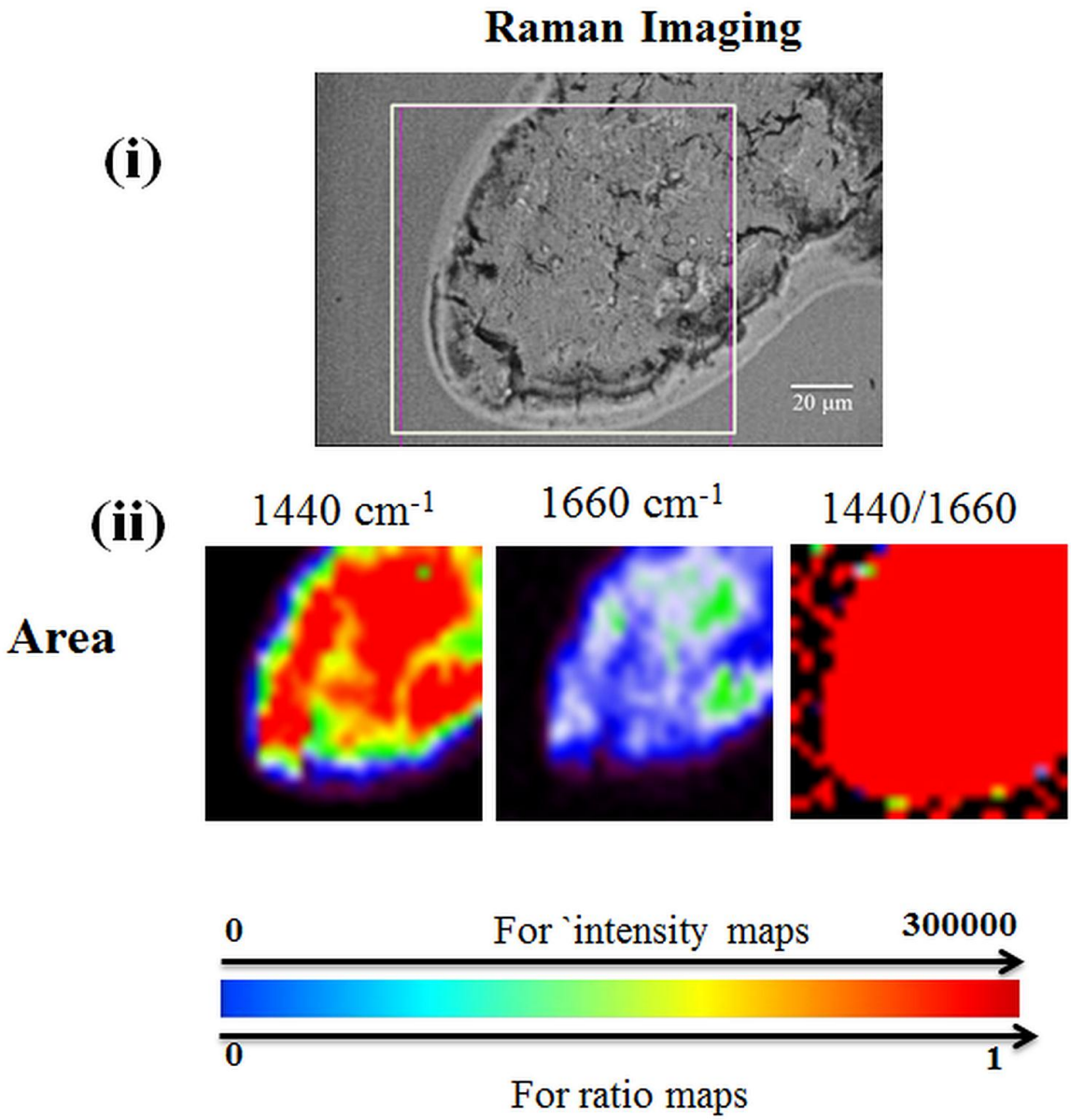
Raman Imaging
(i)
20 µm
(ii)
1440 cm-1
1660 cm-1
1440/1660
Area
0
For `intensity maps
300000
0
1
For ratio maps

Figure 9